Power Electronic Systems
Laboratory

IEEE Journal of Emerging and Selected Topics in Power Electronics, Vol. 10, No. 3, pp. 2989-3012, June 2022

Analysis of the Performance Limits of 166 kW / 7 kV Air-Core and Magnetic-Core Medium-Voltage Medium-Frequency Transformers for 1:1-DCX Applications

P. Czyz,
T. Guillod,
D. Zhang,
F. Krismer,
R. Färber,
J. Huber,
C. Franck,
J. W. Kolar

ETH zürich

Analysis of the Performance Limits of 166 kW / 7 kV Air-Core and Magnetic-Core Medium-Voltage Medium-Frequency Transformers for 1:1-DCX Applications

Piotr Czyz*, *Graduate Student Member, IEEE*, Thomas Guillod*, *Member, IEEE*, Daifei Zhang*, *Student Member, IEEE*, Florian Krismer*, *Member, IEEE*, Jonas Huber*, *Member, IEEE*, Raphael Färber†, *Member, IEEE*, Christian M. Franck†, *Senior Member, IEEE* and Johann W. Kolar*, *Fellow, IEEE*
*Power Electronic Systems Laboratory (PES), ETH Zurich, Switzerland
†High Voltage Laboratory (HVL), ETH Zurich, Switzerland
Corresponding Author: Piotr Czyz (czyz@lem.ee.ethz.ch)

***Abstract*—Solid-state transformers (SSTs) are employing compact high-power medium-voltage (MV) medium-frequency transformers (MFTs) and enable the power transfer between galvanically isolated DC systems. Considering a typical SST isolation stage, i.e., a 166 kW unregulated series-resonant DC-DC converter acting as a DC transformer (DCX) with equal input and output MV DC voltages of 7 kV (1:1-DCX), we derive component-level and system-level performance limits of air-cooled realizations with either an air-core transformer (ACT) or with a magnetic-core transformer (MCT). We describe the design of two fully rated MFT prototypes in detail and provide a comprehensive experimental characterization to validate the derived performance limits, including also the dielectric losses and the analysis of stray magnetic fields. The realized ACT and MCT prototypes achieve measured efficiencies of 99.5 % and 99.7 % at gravimetric power densities of 16.5 kW/kg and 6.7 kW/kg, respectively. Considering 10 kV SiC MOSFETs, calculated system-level efficiencies of the ACT-based and MCT-based 1:1-DCX result in 99.0 % and 99.2 % at the nominal operating point, with similar part-load efficiency characteristics. The paper concludes with an application-oriented qualitative evaluation of the two concepts.**

***Index Terms*—DC transformer (DCX), air-core transformer (ACT), magnetic-core transformer (MCT), medium-frequency (MF), medium-voltage (MV), insulation, solid-state transformers (SSTs).**

I. Introduction

Fuelled by the availability of wide-bandgap (WBG) SiC power semiconductors with blocking voltage ratings of up to 10 kV and beyond, solid-state transformers (SSTs) have been proposed as flexible isolation and voltage-scaling interfaces between medium-voltage (MV) and low-voltage (LV) DC or AC buses. Typical applications include, e.g., hybrid smart grid systems with AC and DC sections [1], [2], grid interfaces for renewable power sources [3], [4], hyperscale data centers [5], [6], high-power electric vehicle (EV) charging stations [7], [8], future ships [9]–[11], and future aircraft with distributed propulsion systems and on-board MVDC grids [12]–[14].

SSTs are comprising compact high-power MV medium-frequency transformers (MFTs) and accordingly enable voltage scaling and power conversion between galvanically separated DC systems. The design of MFTs involves various trade-offs between competing goals (e.g., power density, efficiency, insulation voltage, cost) and a large number of degrees of freedom (e.g., winding and core geometry, insulation material, operating frequency, cooling method) to balance these trade-offs. It is hence a non-trivial process resulting in vastly diversified MFT prototypes as reported in [6], [15]–[27], [27]–[30], [30]–[33], [33]–[50]. **Fig. 1** provides an overview and classification of these MFTs.

Considering certain SST applications (e.g., airborne, marine) and, in general, handling aspects and resource usage, the MFT's gravimetric power density $\gamma = P_\mathrm{N}/m$ (with P_N as the rated power) is an important characteristic. **Fig. 1(b)** indicates $\gamma < \approx 12\,\mathrm{kW/kg}$ for air-cooled (natural or forced convection) MFTs. A first approach to cross this barrier is the use of liquid cooling ($\gamma < \approx 25\,\mathrm{kW/kg}$). However, on the system-level also the mass of the cooling system (heat exchanger, piping, pumps) would need to be accounted for. Furthermore, the relatively high complexity of a liquid cooling system may not be desirable in all applications.

Typically, air-cooled MFTs are realized with magnetic cores (magnetic core transformer, MCT) and a dry-type (potting) insulation system, whose combined mass ultimately limits the achievable gravimetric power density [6], [34], [40]. Thus, a second approach to increase the gravimetric power density beyond this limit requires that neither magnetic cores nor a dry-type insulation system is used. Accordingly, inspired by inductive power transfer (IPT) systems, we have recently proposed a MV air-core transformer (ACT) [13], [48], [51], which utilizes air as insulation medium and for direct cooling of the exposed windings. In addition to high gravimetric power density of up to $\gamma \approx 40\,\mathrm{kW/kg}$, ACTs feature comparably straightforward insulation design and mechanical construction, which, together with the absence of magnetic cores, creates a potential for resource and cost savings. On the other hand, the volumetric power density $\rho = P/V$ of an ACT will be relatively low due to the lack of guidance for the magnetic flux.

This article has been accepted for publication in IEEE Journal of Emerging and Selected Topics in Power Electronics. This is the author's version which has not been fully edited and content may change prior to final publication. Citation information: DOI 10.1109/JESTPE.2021.3123793

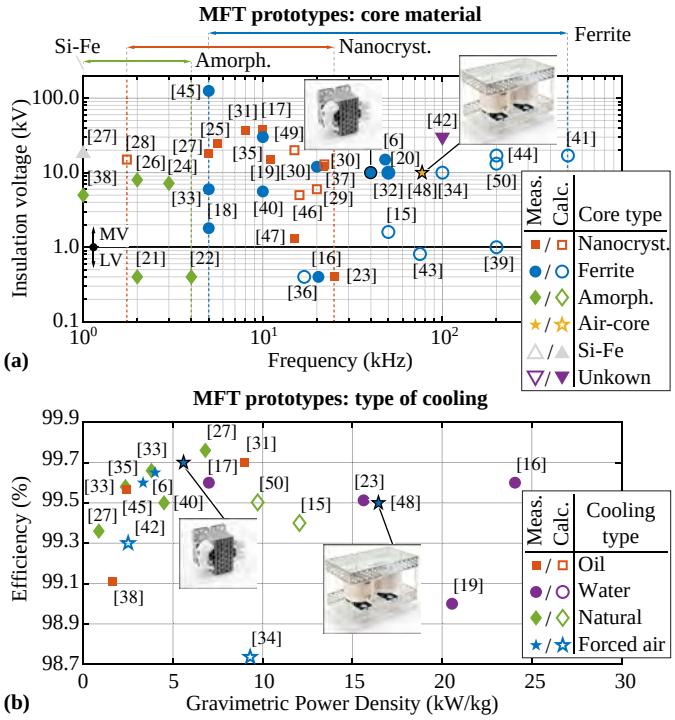

Fig. 1. Overview on MFT prototypes reported in the literature; the two MFTs discussed in this paper are highlighted. **(a)** Rated insulation voltage[a] and operating frequency. Note the frequency-dependence of core material selection. **(b)** Efficiency and gravimetric power density of those prototypes where data on mass was available[b]. Note that the mass of external parts of liquid cooling systems is not considered.

[a] In cases where no explicit insulation voltage rating has been reported, the voltage rating of the high-voltage winding is shown.

[b] Note that information about the masses of prototypes [33], [38], [45], [50] was obtained directly from the authors.

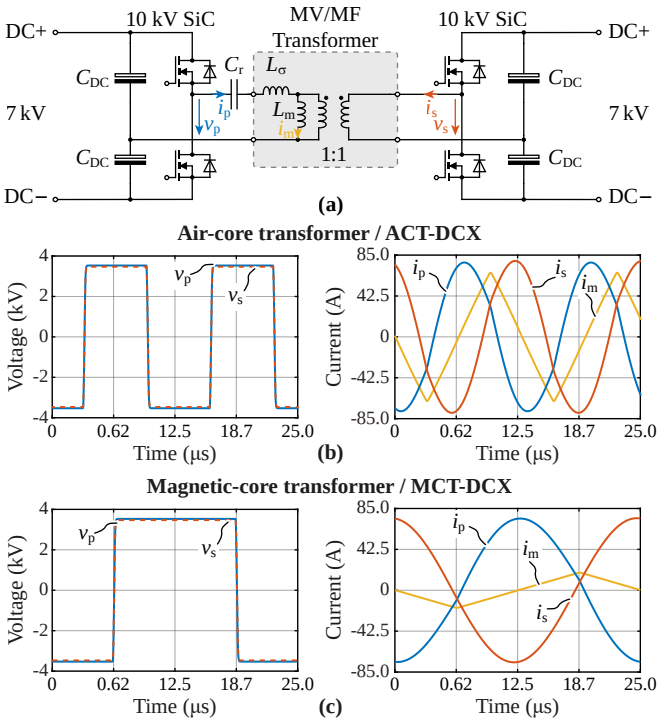

Fig. 2. (a) Converter topology of the considered 166 kW / 7 kV 1:1-DCX. Simulated current and voltage waveforms at rated power and with an operating frequency resulting for optimal designs (**Section II**). **(b)** $f_s = 77.4\,\mathrm{kHz}$ for the ACT. **(c)** $f_s = 40.0\,\mathrm{kHz}$ for the MCT.

TABLE I. Specifications of the 1:1-DCX.

P_N	166 kW	output power
V_{DC}	7 kV(±3.5 kV)	input and output DC voltage
V_i	10 kV DC	pri.-sec. insulation voltage

Whereas the theoretical limits for the volumetric power density of MCTs have been derived in [52]–[54] and a weight-optimized low-power MCT has been presented in [34], to the knowledge of the authors literature does not yet cover a comprehensive and experimentally supported analysis of the gravimetric power density limits of dry-type MCTs and a comparative evaluation against ACTs. Extending and improving the preliminary theoretical analysis from [13], and building on the detailed experimental characterization of an ACT prototype from [48], this paper aims to fill that gap and clarify the comparative evaluation of MCT and ACT concepts. A special focus is placed on the insulation design, the analysis of magnetic stray fields, and the characterization of dielectric losses.

We exemplify the considerations on a 166 kW 1:1-DCX system, i.e., a series resonant DC-DC converter operated at the resonance frequency, which therefore acts as a DC transformer (DCX) [6], [55]–[57]. The DCX tightly couples the DC input and output voltages without the need for closed-loop control. In the case at hand the unity-turns-ratio MFT leads to equal input and output DC voltages of 7 kV, which can be processed with 10 kV SiC MOSFETs, targeting an overall DC-DC efficiency of $\geq 99\,\%$. **Tab. I** summarizes the considered specifications and **Fig. 2** shows the topology and key waveforms. Note that the selected unity ratio of primary-side to secondary-side DC voltages (1:1-DCX) is directly suitable for, e.g., DC bus-tie applications [11] or the coupling of two AC grids [58]. Furthermore, series/parallel associations (e.g., input-series/output-parallel, ISOP) of several 1:1-DCX converter cells facilitate the adaption to different input to output voltage ratios, or to higher overall power or voltage ratings.

The paper is organized as follows: **Section II** describes the detailed modeling and multi-objective optimization of MCT- and ACT-based 166 kW / 7 kV 1:1-DCX converter systems, resulting in the theoretical performance limits for the two concepts on both, the component (MFT) and the system (1:1-DCX) level. **Section III** then discusses realization aspects for both MFTs and constructed prototypes, whereas **Section IV** covers the experimental characterization of a full-scale MCT prototype (for the corresponding characterization of the ACT prototype, we refer to [48]). Thus, **Section V** complements the comparison of theoretical performance limits by a comparative experimental evaluation of full-scale MCT and ACT prototypes, where we focus on the measurement of dielectric losses and overload capability.

Finally, **Section VI** discusses the efficiency characteristics of the MFTs and the complete 1:1-DCXs: at the rated power of 166 kW, the realized MCT and ACT prototypes achieve efficiencies (calculated based on experimentally measured loss components) of 99.7 % and 99.5 % at gravimetric power densities of 6.7 kW/kg and 16.5 kW/kg, respectively. The use of 10 kV SiC MOSFETs enables system-level efficiencies for the MCT-DCX and the ACT-DCX of 99.2 % and 99.0 % at rated power. We conclude the paper with an application-oriented qualitative evaluation of the two concepts and corresponding recommendations.

II. Multi-Objective Optimization

To derive the performance limits (efficiency, gravimetric power density, and volumetric power density) of MCT- and ACT-based 166 kW / 7 kV 1:1-DCX converter systems, we employ the multi-objective optimization approach illustrated by **Fig. 3**, which calculates the performance indices for a wide range of different designs. In general, two separate strategies are employed depending on the transformer type. For the ACT (cf. **Fig. 3(a)**), a 2D-FEM-based optimization is used, which first calculates the electromagnetic fields in the frequency domain, which are then used to calculate the performance indices. For the MCT (cf. **Fig. 3(b)**), we employ a semi-analytical (analytical equations but solved numerically) optimization routine. With the properties of a given transformer design, the system-level performance can be obtained by appropriately dimensioning and modeling the DCX's remaining components (switching stage, resonant capacitors, cooling system).

The following subsections first describe the considered transformer configurations and modeling approaches before then presenting the optimization results and the selection of the designs for the two actually realized prototypes.

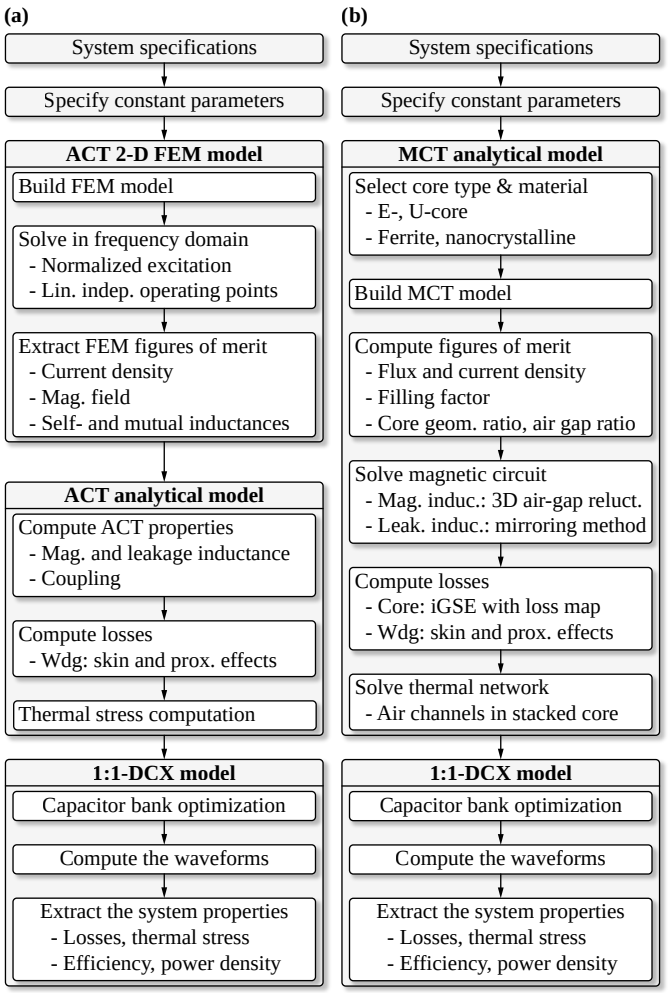

Fig. 3. Optimization flowcharts for **(a)** ACT- and **(b)** MCT-based 1:1-DCX systems.

A. 1:1-DCX Converter Modeling

As mentioned in the introduction and shown in **Fig. 2**, a 1:1-DCX is a series resonant converter. To realize the desired DCX behavior (i.e., a tight coupling of input and output DC voltages in open-loop operation), the resonant tank formed by the transformer's leakage inductance, L_σ, and a series resonant capacitor, C_r, must be tuned such that C_r compensates the leakage inductance at the desired operating (switching) frequency, i.e., $f_\mathrm{s} = f_0 = 1/(2\pi\sqrt{C_\mathrm{r} L_\sigma})$.

With regard to the DC bus voltage of 7 kV and a certain margin regarding the blocking voltage utilization, we consider 10 kV SiC MOSFETs from CREE/Wolfspeed [59], [60]. Note, that the primary and secondary switching stages are built as half-bridges with a split DC-link capacitor to halve the number of switches used (as compared to full-bridge circuits, [28]). We model conduction losses with the on-state resistance at a junction temperature of 125 °C, i.e., 275 mΩ per device (note that a device/package contains two paralleled dies). Making use of the magnetizing current that appears in both, the primary-side and the secondary-side half-bridges, the DCX achieves zero-voltage switching (ZVS) for all operating points [57]. The corresponding residual soft-switching losses, which are non-negligible for the considered switching frequencies, are modeled with experimental data from [61], [62]. **Tab. II** summarizes the key data of the selected semiconductors.

We consider high-power polypropylene capacitors (CELEM CSP120/200 [63]) for the resonant capacitor bank and high-voltage polypropylene capacitors for the DC-link (FTCAP FSP [64]). The losses are calculated via the corresponding dissipation factors. Volume and mass are modeled using the volumetric and gravimetric energy densities of existing prototypes based on these capacitors (see [65] for the resonant capacitors and [6] for the DC-link capacitors). **Tab. II** provides the corresponding data.

Finally, we model volume and mass of the overall converter's forced-air cooling system (i.e., for switching stages, resonant capacitors, and MFT) based on experimental data from [61] and assume a total fan power consumption of 80 W.

B. Air-Core Transformer Modeling

For the sake of clarity, we provide here a brief summary of the ACT model used for the optimization. For an in-depth discussion, please refer to [48].

In [13], [48] we proposed an ACT configuration consisting of two coaxially-arranged, cylindrical primary- and

This article has been accepted for publication in IEEE Journal of Emerging and Selected Topics in Power Electronics. This is the author's version which has not been fully edited and content may change prior to final publication. Citation information: DOI 10.1109/JESTPE.2021.3123793

TABLE II. Parameters used for modeling of the 1:1-DCX components.

SiC MOSFET package with 2 parallel dies		
$V_{\mathrm{ds,max}}$	$10\,\mathrm{kV}$	max. blocking voltage
$I_{\mathrm{ds,max}}$	$2\mathrm{x}18\,\mathrm{A}$	max. drain current
$R_{\mathrm{ds,on}}$	$550/2\,\mathrm{m\Omega}$	on-state res. @ 125°C
P_{max}	$100\,\mathrm{W}$	max. package dissipation
$n_{\mathrm{pack,max}}$	3	max. parallel packages
Resonant capacitors		
$U_{\mathrm{r,max}}$	$10\,\mathrm{kV}$	max. peak voltage
$\tan\delta_{\mathrm{r}}$	$0.05\,\%$	dissipation factor
$e_{\mathrm{r,m}}$	$1\,\mathrm{J/kg}$	gravim. energy density
$e_{\mathrm{r,v}}$	$2\,\mathrm{J/dm^3}$	vol. energy density
DC-link capacitors		
$u_{\%}$	$4\,\%$	peak-peak voltage ripple
$\tan\delta_{\mathrm{link}}$	$0.1\,\%$	dissipation factor
$e_{\mathrm{link,m}}$	$30\,\mathrm{J/kg}$	gravim. energy density
$e_{\mathrm{link,v}}$	$40\,\mathrm{J/dm^3}$	vol. energy density

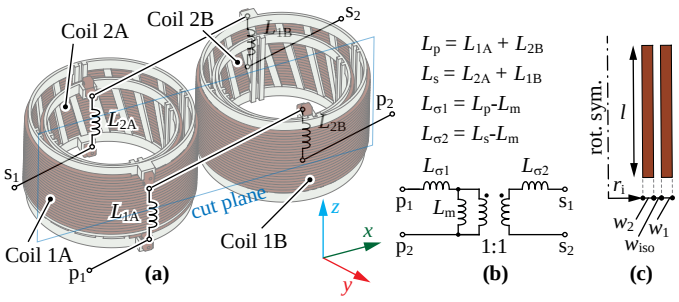

Fig. 4. (a) CAD rendering showing the ACT coil arrangement with coil interconnections: the series connection of $L_{1\mathrm{A}}$ and $L_{2\mathrm{B}}$ forms the primary-side self inductance, L_{p}, and the same applies for the secondary side. **(b)** Lossless linear equivalent circuit of the ACT. **(c)** Simplified 2-D FEM model for one set of coils. Figures from [48].

secondary-side windings, cf. **Fig. 4(a)**. The shown symmetric interconnection of the coils (such that the primary- and the secondary-side windings consist of one outer and one inner coil each) and the selected winding directions achieve partial stray flux cancellation and result in a symmetric linear equivalent circuit (**Fig. 4(b)**) with approximately equal primary- and secondary-side self and leakage inductances, i.e., $L_{\mathrm{p}} \approx L_{\mathrm{s}}$ and $L_{\sigma 1} \approx L_{\sigma 2}$. Note that therefore for the ACT a T equivalent circuit is used (see **Fig. 4(b)**) to highlight the connections and symmetrical physical arrangement, whereas for a generic transformer, where no assumptions regarding symmetry can be made, an equivalent circuit with only three degrees of freedom is used (see **Fig. 2(a)**). Please refer to [66] for a detailed discussion of transformer equivalent circuits. The series resonant capacitor C_{r} is split into two capacitors, $C_{\mathrm{r}1}$ and $C_{\mathrm{r}2}$ (compensating $L_{\sigma 1}$ and $L_{\sigma 2}$, respectively), for ease of realization due to high reactive power and the resulting high capacitor voltages (for further details see **Section III-E**).

Note that even though a partial stray flux cancellation is achieved with the employed coil arrangement, a shielding is advised to limit the magnetic stray flux densities in the proximity of the ACT. We have shown in [48] that for highly efficient and weight-optimized ACTs, a conductive shielding enclosure has negligible effects on the winding losses and on the coupling between the primary-side and secondary-side windings. The shielding design can thus be decoupled from the design of the ACT's active part. Furthermore, the extent to which a shielding must be explicitly placed depends strongly on the location of the ACT in an overall assembly/cabinet. Therefore, we do not consider the shielding during the optimization but discuss a straightforward, low-loss and lightweight solution in **Section III-B**.

Considering specific dimensions of the ACT's coils, a 2-D FEM simulation of the electromagnetic fields of one of the two coaxial coil sets (see **Fig. 4(c)**) is sufficient to parametrize the ACT equivalent circuit from **Fig. 4(b)** and to extract the magnetic fields and the current density required for the calculation of the litz wire (71 µm strand diameter, 39.5 % fill factor) winding losses, which takes high-frequency effects into account according to [67], [68]. The calculated winding losses are increased by $30\,\%$ (loss penalty factor $k_{\mathrm{loss,w}}$) to account for additional losses due to imperfect twisting of litz wires caused by production (mechanical) constraints as during the optimization process the actual construction of the litz wire is not known. The value of this penalty (safety) factor is derived based on empirical data, see [68], [69]. With air as insulation medium, dielectric losses are assumed to be negligible. Furthermore, a simplified thermal model of the ACT relies on a maximum allowable surface-related loss density of $p_{\mathrm{v,max}} = 0.25\ \mathrm{W/cm^2}$ for forced convection cooling of the exposed area of the windings.

The minimum distance between the primary- and the secondary-side windings is fixed to $w_{\mathrm{iso}} = 16.5\,\mathrm{mm}$, which follows from the rated insulation voltage of $V_{\mathrm{i}} = 10\,\mathrm{kV}$ and a (conservative, to account for inhomogeneous field distributions, humidity, etc.) maximum permissible electric field of $0.6\,\mathrm{kV/mm}$ in air. Whereas **Tab. III** summarizes such fixed parameters of the ACT model, **Tab. IV** provides an overview on the design space, i.e., those parameters and their ranges that are varied during the optimization to obtain a wide range of designs. To define different ACT geometries, the following dimensions are varied (see **Fig. 4(c)**):

- internal diameter of the inner coil (r_{i}),
- widths of outer and inner coils ($w_{1,2}$),
- length of coil (l).

In addition, the number of turns (N) and the operating frequency (f_{s}) are varied, too, for each geometry. For further details, please refer to [48].

C. Magnetic-Core Transformer Modeling

As discussed earlier, we consider an air-cooled MCT with a dry-type insulation system. **Fig. 5** shows the three basic arrangements of cores and windings: core-type with U-core, shell-type with E-core, and shell-type with U-core. However, the core-type transformer (cf. **Fig. 5(a)**) uses two sets of windings, which increases the number of cable terminations and leads to a higher complexity of the insulation system, especially in the winding window of the core. Therefore, we consider only the shell-type configurations with E- or U-core for the optimization. We do not consider interleaving

TABLE III. Fixed parameters for ACT and MCT models.

Var.	Value		Description
	ACT	MCT	
Constant parameters			
w_{iso}	16.5 mm	4 mm	insulation distance
d_{litz}	71 µm	71/100 µm	litz strand diam.
k_{litz}	39.5 %	47 %	total litz fill factor
$k_{\text{loss,w}}$	30 %		imperfect twisting loss penalty
$k_{\text{loss,c}}$	–	20 %	core loss map penalty
P_{diel}	0 W	40 W	dielectric losses
$I_{\text{m,peak}}$	N/A	20 A	peak mag. current

TABLE IV. Design space for the 2-D FEM-based ACT optimization.

Var.	Value	Description
f_{s}	[20, 200] kHz	op. frequency
N	[1, 200]	number of turns
r_{i}	[35, 105] mm	inner radius
w_1	[5, 60] mm	width of outer coil
w_2	[5, 60] mm	width of inner coil
l	[60, 700] mm	length of coil

of the primary and secondary windings due to the insulation requirements. To avoid problems with current sharing [70], windings are realized without paralleling of litz wires.

Considering the target operating frequency range of several 10 kHz, the magnetic core can be realized from either ferrite or nanocrystalline material (amorphous cores would yield unacceptable hysteresis and eddy current losses) [54]. By introducing an air gap between the core halves (all limbs), the magnetizing inductance, L_{m}, and hence the magnetizing current available for realizing ZVS of the two converter bridges can be adjusted. The transformer windings are made of litz wires where we consider two different strand diameters (71 µm and 100 µm, 47 % fill factor) to account for the potentially lower operating frequencies compared to the ACT. The minimum insulation distance considered for the MCT is $w_{\text{iso}} = 4\,\text{mm}$, as the windings are encapsulated with silicone elastomer insulation (Dow Corning TC4605 HLV, [71]). Considering that in practical designs part of the inter-winding space is taken by the perforated coil former, the effective distance becomes $2.5\,\text{mm}$ ($1.5\,\text{mm}$ thick coil former) which results in an electric field of $4\,\text{kV/mm}$, well below the silicone's breakdown electric field of $24\,\text{kV/mm}$. Details of the actually realized insulation design and capabilities of the MCT are discussed in **Section III-A**.

We characterize the MCT's performance with analytical models and based on the routine presented in [72], [73]. The magnetic field in the winding window and the leakage inductance L_σ are computed with the mirroring method [74]. Based on the fields, the HF winding losses are analytically computed [72], [74]. Again, the winding loss calculation accounts for imperfect twisting of the litz wire strands with a loss penalty factor $k_{\text{loss,w}} = 30\,\%$, see [68], [69]. The magnetizing inductance L_{m} and the flux inside the core are

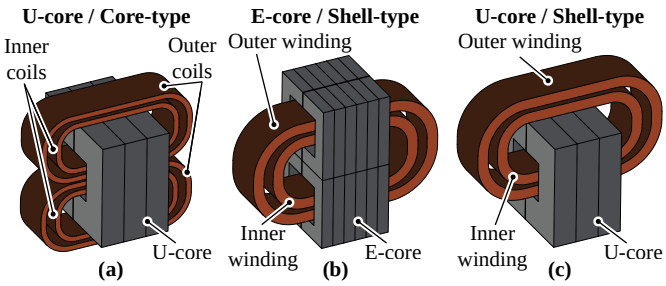

Fig. 5. Considered MCT configurations: **(a)** core-type transformer consisting of an U-core with one set of concentric windings per limb; **(b)** shell-type transformer consisting of an E-core with concentric windings; **(c)** shell-type transformer consisting of an U-core with concentric windings.

obtained with a reluctance model, which considers the air gap fringing field [74], [75]. Furthermore, the core losses are computed with the improved generalized Steinmetz equation (iGSE) [76] using a loss map of the respective core material [77] (function of flux density, frequency, temperature and DC bias). The calculated core losses are increased by 20 % (safety factor $k_{\text{loss,c}}$) to include potential deviations of the employed datasheet-based core loss map from the actual loss density of the cores based on experience from previous prototypes [30], see **Section IV-C2** for experimental validation. Finally, the total dielectric losses of the dry-type insulation system are assumed to be $40\,\text{W}$, which is based on experience from [78]. The thermal management of the transformer is based on heat conduction (from the windings through the dry-type insulation) and forced-air cooling. Thus, the thermal behavior of the MCT can be modeled with a lumped thermal equivalent circuit [77], [79] and it considers thermal and loss coupling between the windings, insulation and core.

Whereas **Tab. III** summarizes fixed parameters of the MCT model, **Tab. V** provides an overview on the design space, i.e., the varying parameters to generate different transformer designs:

- operating frequency (f_{s}),
- core shape, material (3C94 or VITROPERM 500F), dimensions (including the number of stacked cores), and peak flux density (r_{A}, $\hat{B}_{\text{s}}$),
- number of turns and layers in windings (N, N_{layer}),
- current density (J_{litz}),
- air speed (v_{air}) as well as air channel width (d_{air}, for discrete design space only, cf. **Fig. 8(a)**).

Note that for the MCT two design spaces can be distinguished: first, a continuous variation of the core geometry is assumed, i.e., the geometry follows from a variable ratio of core depth to core limb width, r_{A}, the selected winding configuration with insulation that defines the core window height and width, and the necessary total area of the core given by the desired peak flux density. However, in practice only discrete core geometries and litz wire configurations are available off-the-shelf. Therefore, a second optimization run considers only such realizable geometries, whereby several off-the-shelf cores can be stacked to obtain the required total core cross section. Note that, in order to minimize

TABLE V. Analytical design space and constant parameters for the MCT optimization.

Var.	Value		Description
	E-core / U-core		core type
	Ferrite	Nanocrystalline	core material
f_s	[20, 70] kHz	[10, 40] kHz	op. frequency
r_A	[0.3, 2]	[0.3, 1]	core geometry
$\hat{B}_s$	[70, 250] mT	[100, 800] mT	peak flux density
	Shell-type		winding type
J_{litz}	[0.5, 10] A/mm^2		current density
N	[4, 120]		num. of turns
N_{layer}	[1, 3]		num. of layers
v_{air}	[1, 10] m/s		air speed
d_{air}	[0, 4] mm		air channel width

r_A – ratio of the U-core thickness to width of limb

the weight of the core, the length of the individual U-core (along y-axis, cf. **Fig. 8(b)**) is still variable to adapt the winding window optimally to the height of a given winding. Shortening of the limbs can easily be done by the manufacturer and significantly expands the available performance space. Furthermore, introducing air channels between the stacked cores (gapped core, see e.g., **Fig. 8**) improves the heat extraction from the cores [80], [81].

D. Optimization Results

The multi-objective optimization procedure outlined above generates a high number of valid designs of ACT-based and MCT-based 166 kW / 7 kV 1:1-DCX systems. These can be compared regarding their efficiency, gravimetric power density and volumetric power density on both, the component-level (transformers) and on the system-level. Thus, we first present results for component-level optimization outcomes before evaluating the two concepts on the system-level.

1) ACT: The component-level optimization results of the ACT optimization are detailed in [48] and summarized here later in **Fig. 7** to facilitate the comparison against the MCT.

2) MCT: **Fig. 6** compares the different MCT configuration options in the η-γ-performance space (thus emphasizing the aim for a lightweight design). Considering designs using ferrite cores without cooling channels in between (ungapped core), and a conservative airflow velocity of 1 m/s, **Figs. 6(a)–(b)** show that designs based on E-cores and U-cores achieve similar gravimetric power densities that cannot exceed $\gamma < \approx 9\,\mathrm{kW/kg}$, however with a slight advantage of E-core designs in terms of efficiency. **Fig. 6(c)** indicates that replacing the ferrite cores by nanocrystalline cores (while keeping cooling conditions identical) still allows to reach similar yet not significantly better performance. However, the presence of air gaps in nanocrystalline cores is critical regarding losses [82]. Furthermore, owing to the presence of high capacitively coupled voltages in the core, short-circuits can occur between the laminations [83]. Therefore, and because of the scarce availability and high cost of

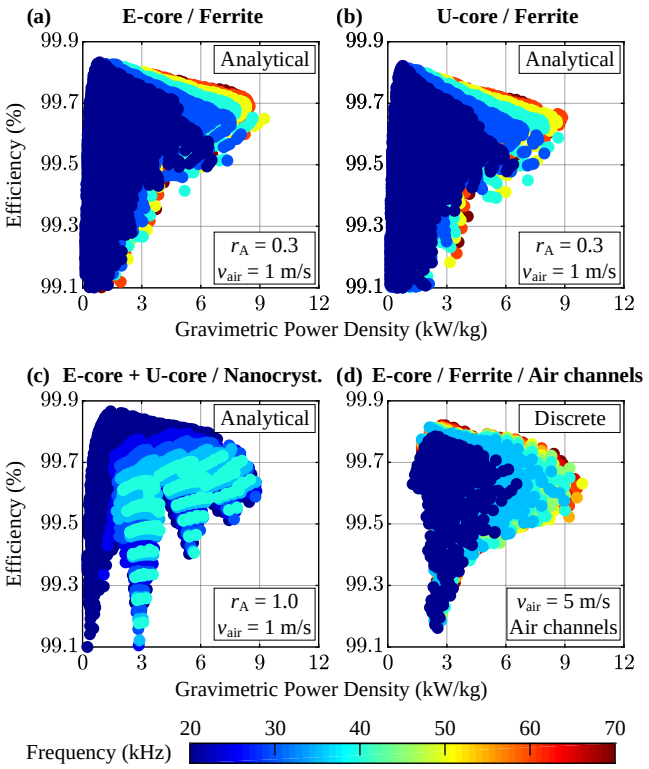

Fig. 6. Results of the multi-objective optimization for different types of the 166 kW / 7 kV MCT, revealing the characteristic dependencies of the η-γ-Pareto fronts on the operating frequency. Results based on the continuous design space showing theoretical limits of realization with ungapped cores and conservative cooling (1 m/s airflow): **(a)** ferrite E-core type; **(b)** ferrite U-core type; **(c)** nanocrystalline E- and U-core types. **(d)** Results based on off-the-shelf components (discrete design space) for the selected concept of ferrite E-core type with air channels between the stacked cores (gapped) to improve the cooling capabilities (5 m/s airflow).

nanocrystalline cores, we do not consider this core material further.

Aiming for an actual realization of an MCT prototype, we consider a discrete design space comprising actually obtainable cores and litz wires. With the same boundary conditions as used for the idealized results (continuous design space) shown in **Figs. 6(a)**, **(b)**, the maximum gravimetric power density of designs obtained from the discrete design space is limited to $\gamma < \approx 5\,\mathrm{kW/kg}$. To prevent this significant reduction, we insert air channels between the stacked cores [80], which improves the heat extraction. Increasing in addition the airflow velocity to still moderate 5 m/s facilitates the performance shown in **Fig. 6(d)**, which is similar to the earlier results. Further increasing the airflow velocity results in diminishing improvements only but clearly requires higher effort (larger and more powerful fans), which is why we consider 5 m/s suitable for practical realizations. Thus, the maximum gravimetric power density of practical MCT designs can reach $\gamma = 10\,\mathrm{kW/kg}$. We consider the results of this discrete design space based on ferrite E-cores for the comparison with the ACT below.

Note that the above considerations highlight the importance of considering real dimensions of available components, mainly of the magnetic cores, during the optimization

This article has been accepted for publication in IEEE Journal of Emerging and Selected Topics in Power Electronics. This is the author's version which has not been fully edited and content may change prior to final publication. Citation information: DOI 10.1109/JESTPE.2021.3123793

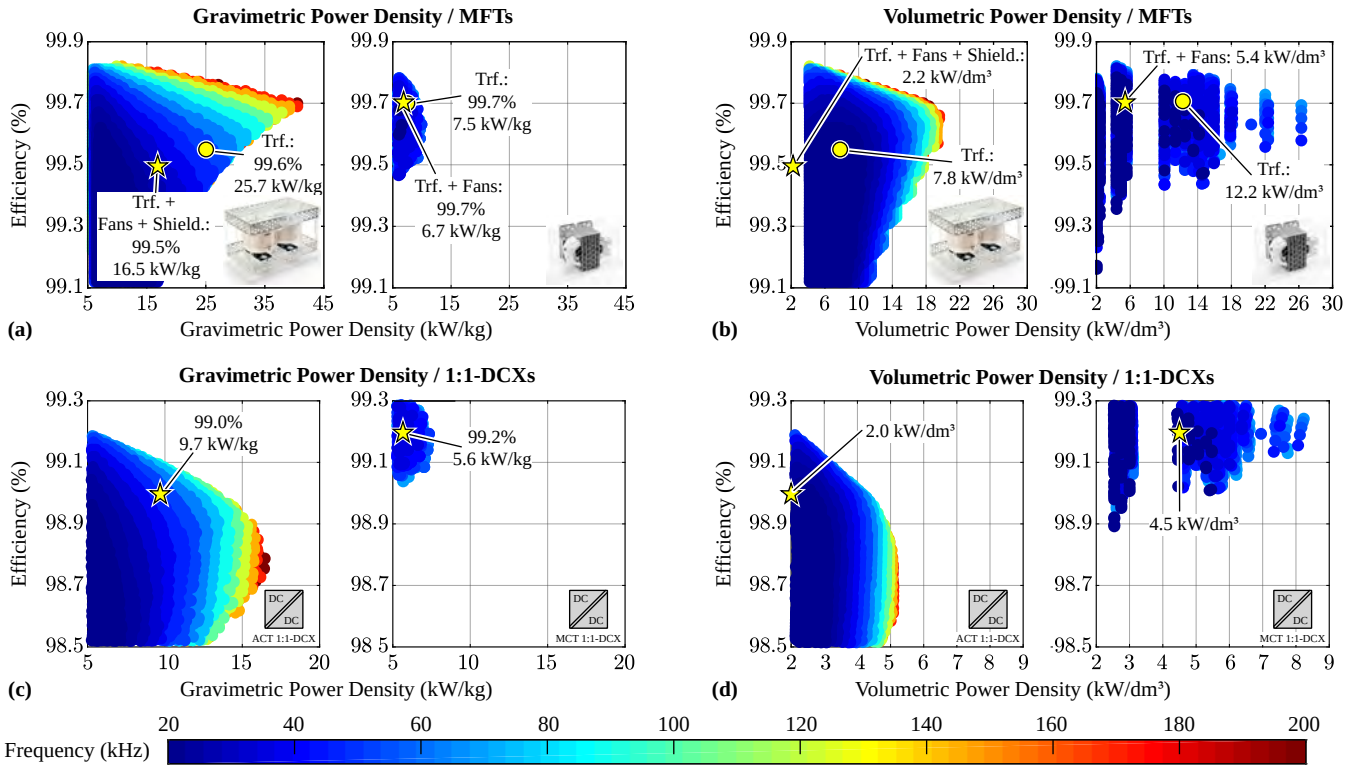

Fig. 7. Results of the multi-objective optimization of the ACT- and MCT-based 166 kW / 7 kV 1:1-DCX. **(a)** Component-level (ACT and MCT) efficiency vs. gravimetric and **(b)** vs. volumetric power density; **(c)** system-level DC-DC efficiency vs. gravimetric and **(d)** vs. volumetric power density of the ACT-DCX and MCT-DCX. The markers ○ represent the selected designs and the markers ☆ indicate measured results of the actually realized MFT prototypes ($f_s = 77.4\,\mathrm{kHz}$ for the ACT; $f_s = 40.0\,\mathrm{kHz}$ for the MCT). Note that their performance deviations from the optimization results exist because of additional constructive constraints and because the idealized models did not yet include weight and volume of the cooling system (fans) and of the aluminum conductive shielding of the ACT.

of MCTs. No such restrictions exist for the design of ACTs (except regarding available litz wires).

3) System-level comparison of ACT- and MCT-DCX: **Fig. 7** shows the η-γ-ρ-performance spaces and thus unveils the performance limits of the optimized ACT and MCT (**Figs. 7(a), (b)**) and of the overall ACT- and MCT-1:1-DCXs (**Figs. 7(c), (d)**). On the system-level, the η-γ-performance planes from **Figs. 7(a), (c)** show that the MCT-DCX cannot achieve a power density of more than $7.5\,\mathrm{kW/kg}$ due to thermal limitation of the MCT. In contrast, the ACT-DCX can achieve twice the gravimetric power density, i.e., up to $16\,\mathrm{kW/kg}$, while maintaining a lower but still comparably high DC-DC efficiency of $98.9\,\%$. It is worth to point out that even though there are highly efficient ACT designs ($99.7\,\%$, cf. **Fig. 7(a)**), a high operating frequency up to $200\,\mathrm{kHz}$ is required. As this leads to high switching losses of SiC MOSFETs, those designs have poor system-level performance (cf. **Figs. 7(c)**). Similarly, the higher maximum system-level efficiency of the MCT-DCX follows from the lower operating frequencies and lower magnetizing current of typical MCTs.

The picture reverses when considering the volumetric power density: **Fig. 7(b)** reveals that on the component-level, the ACT is limited to $\rho < \approx 19.5\,\mathrm{kW/dm^3}$, and more compact realizations (up to $26\,\mathrm{kW/dm^3}$) can be achieved with the MCT. This trend is even more pronounced on the system-level, for which **Fig. 7(d)** indicates maximum volumetric power densities of $8.2\,\mathrm{kW/dm^3}$ for the MCT-DCX compared to $5.2\,\mathrm{kW/dm^3}$ for the ACT-DCX. In addition, note that these results do not yet include a shielding enclosure of the ACT (see **Section III-B**), which would significantly increase the overall boxed volume. This can also be seen from the two markers that indicate the predicted performance of the selected designs and the actually measured values of the realized MFT prototypes.

4) Design selection for realization: We select the ACT and MCT designs to be realized as prototypes by demanding a system-level DC-DC efficiency of $\geq 99.0\,\%$ and then choosing the MFT design with highest calculated (component-level) gravimetric power density. The selected designs are indicated in **Fig. 7**. In case of the ACT, note that even though very high switching frequencies would result in highest component-level performance, the frequency must remain below $100\,\mathrm{kHz}$ to achieve the system-level efficiency target by limiting the switching losses of the power semiconductors. This constraint together with the availability of only discrete capacitance values of high-power resonant capacitors led us to the selection of a design with an operating frequency of $f_s = 77.4\,\mathrm{kHz}$. As **Fig. 6(d)** indicates, there is no significant benefit of increasing the MCT operating frequency above $40\,\mathrm{kHz}$ (e.g., to $70\,\mathrm{kHz}$), which is thus selected.

Note that various practical aspects and mainly mechanical constrains (see **Section III**) typically decrease the power

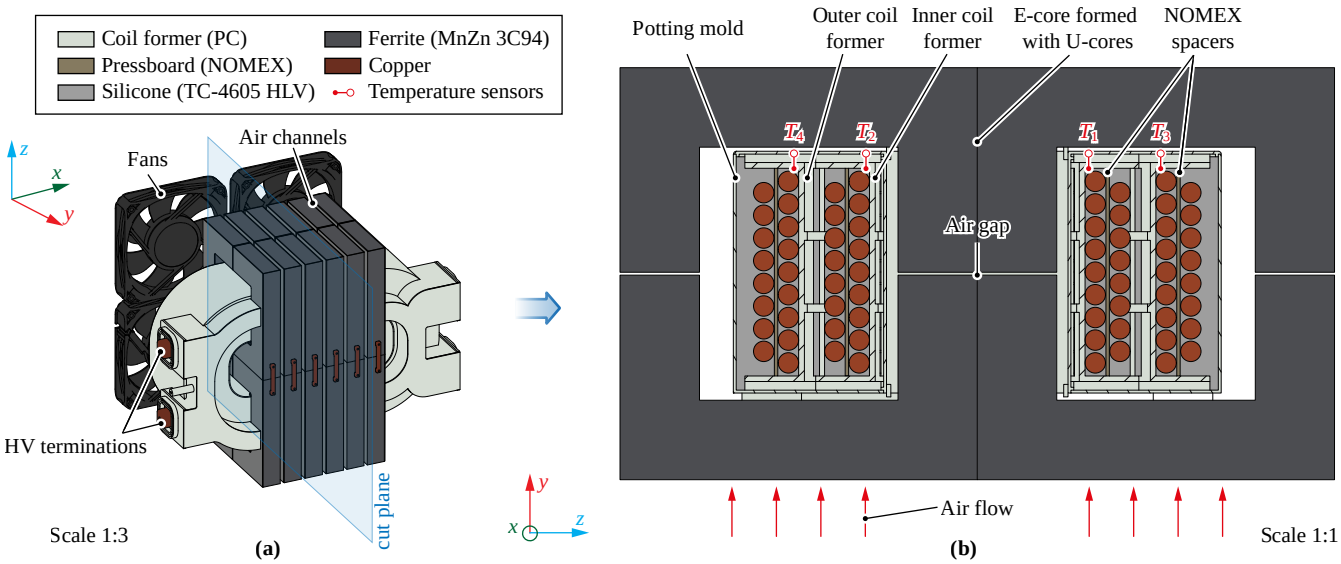

Fig. 8. **(a)** 3-D CAD rendering of the MCT prototype showing winding package (terminations, polycarbonate cover), cores with air channels, and cooling fans. **(b)** Cut view of the transformer. The direction of the airflow as well as the positions of temperature sensors used during characterization are indicated. Note the Nomex spacers that are used to maintain a distance of at least 1.5 mm between the layers of the windings.

density of prototypes compared to idealized calculation results. This explains why the realized prototypes do not lie on the η-γ-Pareto front, see **Figs. 7(a), (b)** and **Section VI** for details.

III. Design and Construction

As mentioned above, the ultimately achievable mass and volume of the selected ACT and MCT designs (and, because the MFTs contributions dominate the entire DCX systems) strongly depend on practical realization aspects. Therefore, this section presents the design and construction of the two transformer prototypes, focusing on the key aspects of insulation design, shielding of electromagnetic stray fields and cooling. Furthermore, the realization of the resonant capacitor banks as well as of the switching stages is briefly described.

A. MFT Insulation Design

For both transformers, the rated CM DC insulation voltage is $V_\mathrm{i} = 10\,\mathrm{kV}$. According to IEC 62477 [84], [85], the minimum required clearance distance for overvoltage category III (OV-III), which demands an impulse withstand voltage of 37 kV, becomes 55 mm. Similarly, the minimum required creepage distance, considering pollution degree 2 (PD2) and insulation material group II, is 71 mm.

Regarding the overall mechanical arrangement of the ACT, **Fig. 4** shows how the single-layer winding of each coil is placed on an individual 3D-printed polycarbonate coil former. A fixed insulation distance ($w_\mathrm{iso} = 16.5\,\mathrm{mm}$) between the primary- and the secondary-side windings has been considered already during the optimization, limiting the field strength in the air between the windings to safe values ($< 0.6\,\mathrm{kV/mm}$ considering homogeneous field). In order to realize the required clearance and creepage distances, cylindrical barrier elements made of $1.5\,\mathrm{mm}$ type 993 Nomex pressboards are placed between the primary- and secondary-side coils. Similarly, a rectangular Nomex plate (thickness of $1.5\,\mathrm{mm}$) ensures sufficient clearance between the two coil sets. We realized a creepage distance of $79\,\mathrm{mm}$. The implemented clearance distance of $66\,\mathrm{mm}$ corresponds to an impulse withstand voltage of about 43 kV. Note that this relatively simple insulation system allows to tailor clearance and creepage distances as required by standards and environmental conditions a-posteriori (i.e., after the optimization) by adapting the dimensions of the Nomex elements, with little impact on the overall mechanical design.

Fig. 8 shows a 3-D CAD rendering of the MCT prototype which consists of a ferrite E-core (assembled from 24 ferrite U126/72/20 U-cores), and a winding package. The winding package contains two (primary and secondary) two-layer coils that are wound on corresponding coil formers, encapsulated in a dry-type (silicone) insulation and enclosed by a 3D-printed polycarbonate cover. The realized minimum distance between the primary- and the secondary-side is $w_\mathrm{iso} = 6\,\mathrm{mm}$, which is higher than the value used during the optimization ($w_\mathrm{iso} = 4\,\mathrm{mm}$, see **Section II-C**). This is necessary because of the increased dimensions of the coil formers needed to provide sufficient rigidity to facilitate the manufacturing of the windings using relatively thick litz wire. The windings are encapsulated (potted) with a two-component silicone compound (TC4605 HLV, [71]) that is characterized by a relatively low dissipation factor and a high thermal conductivity. With the insulation distance $w_\mathrm{iso} = 6\,\mathrm{mm}$ and the considered insulation voltage of $10\,\mathrm{kV}$, the electric field in the insulation becomes $1.7\,\mathrm{kV/mm}$, which is significantly below the breakdown electric field of the silicone ($24\,\mathrm{kV/mm}$). The realized clearance distance is the same as for the ACT ($66\,\mathrm{mm}$, impulse withstand voltage of about 43 kV). The creepage distance is much longer, i.e., about $200\,\mathrm{mm}$, owing to the realized creepage

This article has been accepted for publication in IEEE Journal of Emerging and Selected Topics in Power Electronics. This is the author's version which has not been fully edited and content may change prior to final publication. Citation information: DOI 10.1109/JESTPE.2021.3123793

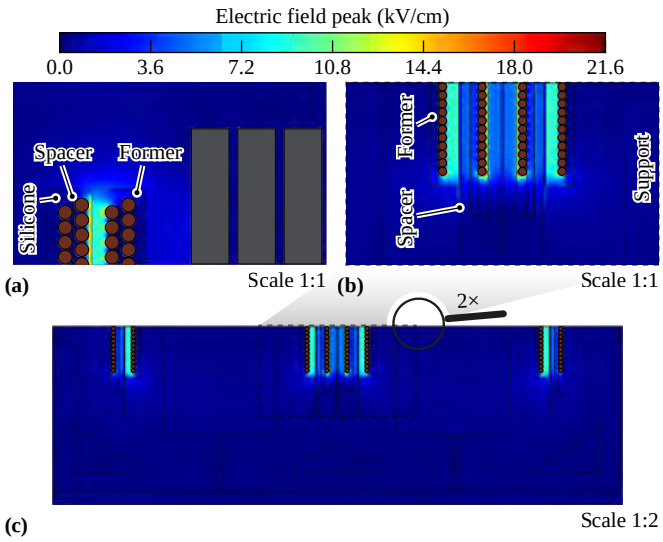

Fig. 9. Cross sectional views of 3D-FEM simulations of the electric field distribution (peak values) in the transformers for the worst-case operating point with $+5\,\mathrm{kV}/{-5\,\mathrm{kV}}$ CM excitation: **(a)** MCT, **(b)** ACT (magnified partial view of the middle of the transformer), and **(c)** ACT (complete cross section view).

distance extenders surrounding the terminations, which are integrated into the polycarbonate cover of the winding package, see **Fig. 8(a)**.

From the peak voltage applied to a winding of the transformer, which is the difference of the voltage applied by a half-bridge ($v_{\mathrm{p,s}}$) and the voltage of the corresponding resonant capacitor (v_{Cr} in case of the MCT or $v_{\mathrm{Cr1,Cr2}}$ in case of the ACT), the maximum voltage between two adjacent turns of a coil can be obtained. This voltage is about $5.4\,\mathrm{kV}/44 \approx 123\,\mathrm{V}$ for the ACT and about $4.0\,\mathrm{kV}/17 \approx 235\,\mathrm{V}$ for the MCT. Both values are well below the capability of the litz wire's insulation, i.e., a double layer of polyamide. As the MCT uses a two-layer winding, the worst-case voltage between the two layers is $2.0\,\mathrm{kV}$, resulting in an electric field of $1.3\,\mathrm{kV/mm}$. Thus, the insulation between the two layers is ensured by $1.5\,\mathrm{mm}$ Nomex spacers (electric strength of $34\,\mathrm{kV/mm}$).

The winding terminations of both prototypes are copper blocks that are edgeless (i.e., feature rounded edges) to prevent excessive local electric fields in the surrounding air.

We employ 3-D FEM simulations of the electric fields inside the transformers for a final verification of the insulation design for the CM voltage of $+5\,\mathrm{kV}/{-5\,\mathrm{kV}}$. The structural and insulation materials are modeled using the dielectric parameters given in **Section V-A**. The results for the MCT shown in **Fig. 9(a)** indicate a maximum peak value of the electric field in the inter-winding space of $E_{\mathrm{peak,max}} = 17.0\,\mathrm{kV/cm}$, which is more than $14\times$ lower than the breakdown field strength of silicone ($240\,\mathrm{kV/cm}$). **Fig. 9(b), (c)** show the results for the ACT, where a maximum peak value of the electric field of $E_{\mathrm{peak,max}} = 21.3\,\mathrm{kV/cm}$ is found around the wires. This value is lower than the critical field strength of dry air ($24.4\,\mathrm{kV/cm\,bar}$).

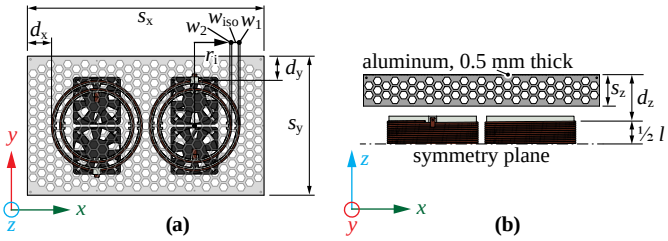

Fig. 10. Simplified 3-D CAD model showing conductive aluminum shielding featuring a honeycomb pattern of holes: **(a)** top view, **(b)** side view. Figures from [48].

TABLE VI. Specifications of the conductive aluminum shielding.

Dimensions of shielding (in mm)		
$d_{\{\mathrm{x,y,z}\}}$	$\{60.5, 60.5, 126.0\}$	distance from coils
$s_{\{\mathrm{x,y,z}\}}$	$\{601, 353, 80\}$	width, depth, height
t_{sh}	$0.5\,\mathrm{mm}$	thickness of wall

B. MFT Shielding

In [48], we have described the design of a lightweight, low-loss conductive shielding to limit the magnetic stray fields in the vicinity of the ACT to safe levels according to the ICNIRP 2010 guidelines [86]. A conductive shielding (cf. **Fig. 10** and **Tab. VI** for dimensions) allows for eddy currents to flow such that they, according to Lenz's law, (partially) compensate the stray magnetic field. Of course, these eddy current generate losses; however, a quite thin (e.g., $0.5\,\mathrm{mm}$) aluminum sheet provides sufficiently low resistances to limit these to reasonable values of about 50 W (estimated with 3-D FEM simulations). Using a honeycomb perforation of the shielding facilitates forced-air cooling and decreases the weight without compromising the shielding efficacy. Note that for the prototype, we realize only a partial shielding covering the worst-case regions with respect to magnetic stray fields (see **Fig. 13(b)**). This simplifies experimental testing as the access to the windings remains free.

Even though magnetic-core MFTs commonly are not shielded [6], [15]–[27], [27]–[30], [30]–[33], [33]–[47], [49], [50], it has been shown that the magnetic flux density in the proximity of MCTs, especially close to the air gap, can reach up to several mT [87], causing eddy-current losses in metallic elements and disturbances in nearby electronic circuitry [88], [89]. It is therefore interesting to analyze the magnetic stray fields of the MCT prototype and to compare them against the ICNIRP guidelines [86] and the results for the ACT, thereby clarifying whether additional shielding is necessary.

Figs. 11(a)–(b) show the simulated (3D-FEM) rms flux densities in the proximity of the MCT and of the ACT, respectively, for their nominal currents and without shielding, and **Figs. 11(c)–(d)** present respective values of the magnetic flux densities at the observation points $1\ldots8$ along the x- and z-axis. Close to the MCT, the stray flux density in the plane of the air gap is similarly high as that of the ACT, however, decays faster with increasing distance. Thus, the ICNIRP [86] limit for occupational exposure is met at a

This article has been accepted for publication in IEEE Journal of Emerging and Selected Topics in Power Electronics. This is the author's version which has not been fully edited and content may change prior to final publication. Citation information: DOI 10.1109/JESTPE.2021.3123793

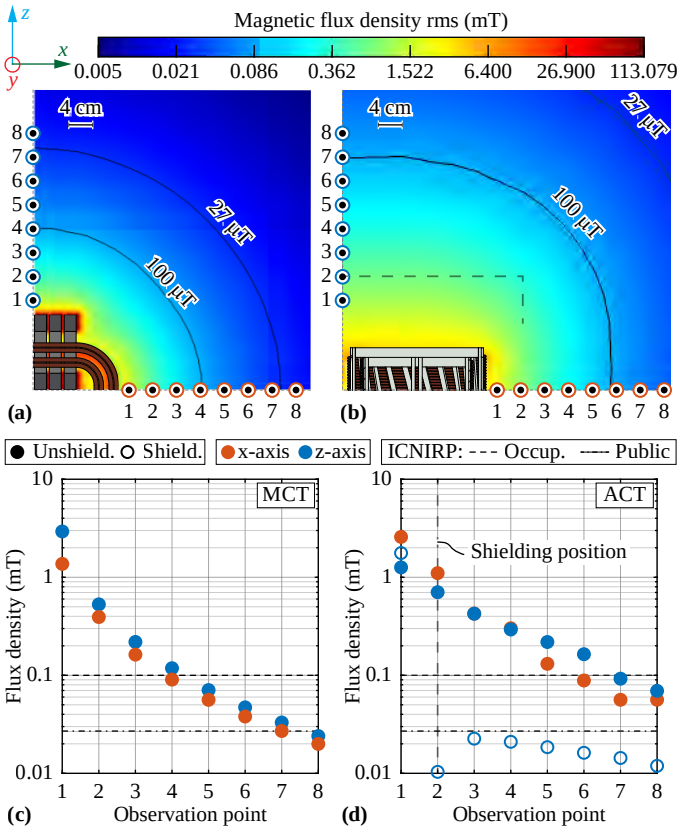

Fig. 11. Magnetic flux densities (rms) for nominal winding currents obtained from 3D-FEM simulations: **(a)** MCT (plane of an air gap), **(b)** ACT (without shielding, plane through middle of coils). **(c)**–**(d)** Respective values of the mag. flux densities at the indicated observation points 1…8. Additionally, the shielding efficacy along the z-axis for the ACT is visualized for comparison (non-filled circles). The ICNIRP 2010 [86] exposure limits for the general public (27 µT) and personnel in occupational settings (100 µT) are indicated, too.

distance of about 130 mm from the MCT, in both, x- and z-directions (cf. points 4). The stray field decays below the limit for the exposure of the general public at a distance of about 250 mm. Note that the respective threshold distances for the (unshielded) ACT are 210 mm and 370 mm (beyond the range shown in **Fig. 11(b)**), i.e., significantly higher, which makes explicit shielding necessary.

We thus conclude that in contrast to the ACT, the MCT does not require additional shielding of magnetic stray fields, as 250 mm seems a reasonable minimum distance between persons and an MV system also for reasons of electrical safety. However, two relatively simple methods to shield magnetic stray fields of an MCT exist, i.e., to use an air gap in the center leg (of an E-core) only or to wrap a thin copper foil around the core. The latter is known as *flux band* or *bellyband* and is common in audio or safety isolation transformers. Furthermore, such a copper band can also serve a second purpose and be used to define the electrical potential of the magnetic cores, e.g., by connecting them to safety ground.

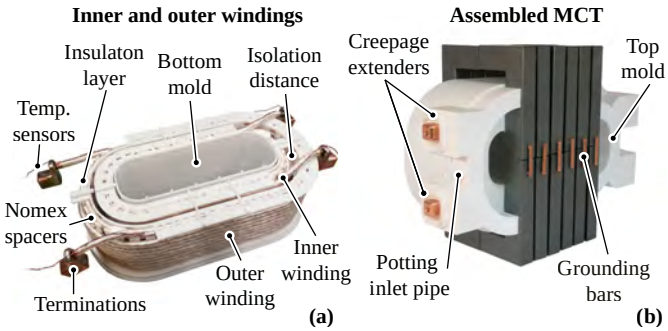

Fig. 12. **(a)** Photos of the realized windings of the MCT (before potting) and **(b)** final assembly without the cooling system.

C. MFT Cooling

Both transformers employ forced-air cooling with identical sets of four fans (4×12 W, 4414FNH).

To improve heat extraction from the ACT's windings, the coil formers are perforated (see **Fig. 4(a)**), which increases the winding surface that is directly exposed to the airflow generated by the fans placed below the transformer. For further details, please refer to [48].

In contrast, the extraction of losses from the MCT windings is hindered by the dry-type insulation, despite the relatively high thermal conductivity of the chosen silicone material. Therefore, a design with low winding losses is preferred as the heat can be much easier extracted from the cores. Placing 4 mm wide air channels between the stacked core sets significantly increases the core and winding package surface areas available for cooling. Furthermore, the transformer is oriented with the largest core surface (xz-plane, cf. **Fig. 8**) facing the airflow (along y-axis), ensuring also symmetric cooling conditions of the winding package.

D. Realized MFT Prototypes

Fig. 12 presents photos of the MCT's windings before potting and of the assembled MCT without the cooling system. It can be seen that the windings are placed on 3-D printed coil formers which are perforated (cf. **Fig. 12(a)**) to facilitate the silicone's flow during the vacuum pressure potting [6]. Furthermore, 2 NTC temperature sensors (PS104J2) are placed close to the endings of both, inner and outer, windings. **Fig. 12(b)** presents the assembled MCT and the remaining features such as potting pipes, creepage extenders and grounding bars.

The complete MCT and ACT prototypes including the cooling systems are shown in **Fig. 13**. **Tab. VII** gives an overview on the key characteristics of the realized prototypes.

E. Resonant Capacitor Banks

As discussed earlier, the required series resonant capacitance must compensate the transformer's leakage inductance at the target operating frequency, i.e., $C_\mathrm{r} = 1/((2\pi f_\mathrm{s})^2 L_\sigma)$. Thus, we obtain $C_\mathrm{r} = 41$ nF for the ACT and $C_\mathrm{r} = 300$ nF for the MCT.

In case of the MCT, the resulting peak resonant capacitor voltage of 1.0 kV facilitates a compact realization on one

TABLE VII. Key characteristics of the realized 166 kW / 7 kV magnetic-core (MCT) and air-core (ACT) transformer prototypes and their resonant capacitor banks.

	MCT	ACT	
Equivalent circuit parameters			
L_σ	52.4 µH	2×51.8 µH	pri. / sec. leak. induc.
L_m	1.18 mH	162.6 µH	magnet. inductance
n	1 : 1		turns ratio
k	0.98	0.76	coupling factor
$I_\mathrm{p,s}$	52.4 A	56.6 A	pri. / sec. rms current
I_m	10.3 A	40.0 A	magnet. rms current
Winding			
N	17	2×22	number of turns
Litz wire	$5 \times 6 \times 5 \times 36$	$5 \times 10 \times 40$	bundles / strands
	double layer polyamide		insulation of litz wire
d_litz	71 µm		single strand diameter
n_litz	5400	2000	number of strands
J_litz	2.5 A/mm^2	7.2 A/mm^2	current density
Core			
N	24× U126/72/20	–	ferrite material 3C94
d_gap	2×1.1 mm	–	air gap
Insulation			
	dry-type	air	type
V_i	10 kV	10 kV	DC insulation voltage
w_iso	6 mm	16.5 mm	insulation distance
Resonant capacitor bank			
f_s	40 kHz	77.4 kHz	operating frequency
C_r	300 nF	2×81.6 nF	resonance cap.

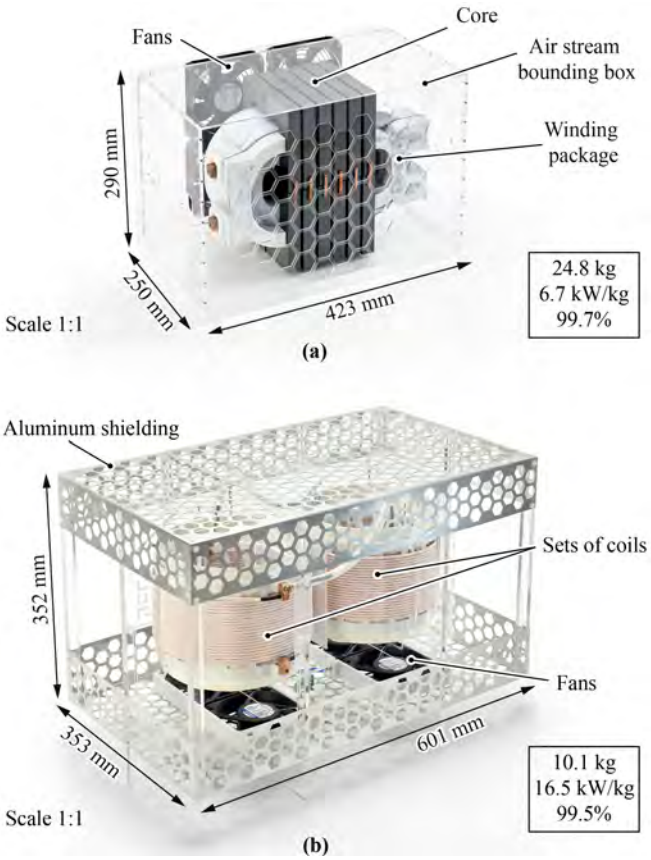

Fig. 13. Photo of the realized 166 kW / 7 kV **(a)** magnetic-core transformer (MCT), **(b)** air-core transformer (ACT).

side of the transformer, using ceramic C0G capacitors (4 series × 12 parallel CGA9 100 nF), see **Fig. 14(a)**. The designed PCB offers the flexibility to configure a large number of individual capacitors in a series-parallel arrangement. It is therefore not optimum in terms of size, yet its volume and mass are still negligible compared to the MCT.

In contrast, the peak capacitor voltage in case of the ACT would reach 4.0 kV if a single component were used. Therefore, to reduce the component stress and facilitate meeting the necessary clearance and creepage distances, we split C_r into two capacitor banks $C_\mathrm{r1} = C_\mathrm{r2} = 82$ nF that are placed on either side of the transformer (cf. **Section II-B**). Still, the capacitors process high reactive power and high currents. Therefore, we realize them with polypropylene capacitors (each with 3 series-connected 240 nF CELEM CSP120/200). Since the expected losses are substantial (see **Section VI-A** for the discussion of losses), they require a cooling system consisting of heatsinks and fans as shown in **Fig. 14(b)**. The cooling system is optimized to minimize the mass according to [90], whereas the thermal modeling of capacitors is based on [91]. The contribution to the overall volume and mass is clearly higher compared to the capacitor bank required for the MCT-based system.

F. Switching Stages and DC-link Capacitors

Each switching stage consists of a MOSFET half-bridge and two DC-link capacitors (C_DC). Note that we did not actually build these switching stages due to the associated high cost and limited availability of the 10 kV switches, and because of the limited additional insight with respect to the MFTs that could be gained. Nevertheless, the volume, mass and losses of their components can be reliably estimated based on the models discussed above and earlier prototype systems [6].

The required capacitance C_DC is 1.3 µF and 2.3 µF for the ACT- and MCT-DCX, respectively, and it is obtained based on the specified maximum peak-peak voltage ripple, see **Tab. II**. The difference follows from the two different switching frequencies of 77.4 kHz and 40 kHz, respectively.

Note that because of the higher operating frequency and also because of the higher rms current in case of ACT-DCX, the switching stages require a higher total chip area (more dies in parallel per switch). Consequently, 6 parallel dies (3 packages) are needed for the ACT-DCX, whereas 4 parallel dies (2 packages) are sufficient for the MCT-DCX.

IV. Experimental Characterization of the MCT

Whereas the characterization of the ACT prototype (cf. **Fig. 13(b)**) has been reported in detail in [48], this

This article has been accepted for publication in IEEE Journal of Emerging and Selected Topics in Power Electronics. This is the author's version which has not been fully edited and content may change prior to final publication. Citation information: DOI 10.1109/JESTPE.2021.3123793

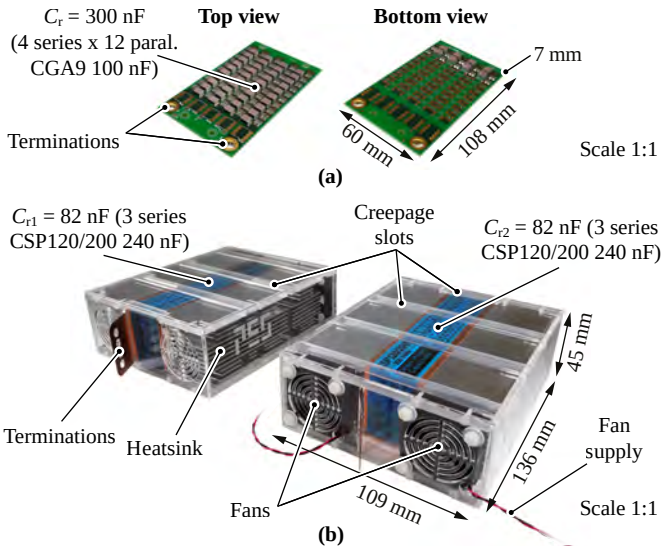

Fig. 14. Photos of the realized resonant capacitor banks: **(a)** C_r for the MCT; **(b)** C_{r1} and C_{r2} for the ACT. Note that due to lower reactive power and hence losses, the ceramic capacitors (C_r for the MCT) do not require active cooling.

TABLE VIII. Small-signal parameters of the MCT (determined at $f = 40\,\mathrm{kHz}$).

Param.	Analyt.	Sim. 3-D	Meas.	Dev. Analyt. \ 3-D
L_σ	47.7 µH	50.0 µH	52.5 µH	9.0 % \ 4.8 %
L_m	1.13 mH	1.23 mH	1.18 mH	4.3 % \ 4.0 %
k	0.96	0.98	0.98	1.9 % \ 0.2 %

section summarizes the corresponding experimental characterization of the MCT prototype shown in **Fig. 13(a)**, i.e., experiments covering small-signal impedance measurements, insulation tests, large-signal tests, winding and core loss measurements, transient thermal response characterization, and magnetic stray flux density measurements. These results together with those for the ACT from [48], as well as further comparative experimental analysis of specialized aspects such as the dielectric losses, given in **Section V**, provide a comprehensive verification of the system-level comparison of ACT-DCX and MCT-DCX concepts given in **Section VI**.

A. Impedance Measurements and Resonances

We measure the MCT's short-circuit and open-circuit impedances from the primary and from the secondary side with a precision impedance analyzer (Agilent 4924A) to validate the computed values of L_σ and L_m from the equivalent circuit of **Fig. 2(a)**. **Tab. VIII** compares the simulated and the measured values at the operating frequency of $40\,\mathrm{kHz}$. All deviations between measurements and simulations are below $9\,\%$, confirming good accuracy of the models employed for the optimization. **Fig. 15** shows the frequency characteristics of the open- and short-circuit impedances of the MCT as well as the common-mode (CM) impedance across the galvanic insulation (measured between the shorted primary-side winding and the shorted secondary-side winding). The CM capacitance of $190\,\mathrm{pF}$ is relatively low, yet higher than that of the ACT ($102\,\mathrm{pF}$).

To check for any undesired impact of the resonances observed from **Fig. 15**, we compare the first series resonance frequency with the envelope of the PWM voltage applied to the transformer, as suggested in [92]. The spectral envelope of a symmetric PWM voltage with a fundamental period of $T_s = 1/f_s$ and equal rise time (t_r) and fall time (t_f), see **Fig. 2**, can be described by the two corner frequencies $f_{c,1} = 1/\pi T_s$ and the higher $f_{c,2} = 1/\pi t_r$. For $f > f_{c,2}$, the envelope decays with $-40\,\mathrm{dB/dec}$. Even for very short rise/fall times of $t_r = t_f = 200\,\mathrm{ns}$, we find $f_{c,2} = 1.6\,\mathrm{MHz}$, which is lower than the MCT's first series resonance frequency of $1.73\,\mathrm{MHz}$ (as short-circuit resonances have even higher values, see **Fig. 15**). Therefore, the resonances are uncritical with regard to the operation of the 1:1-DCX.

B. Large-Signal Tests

As outlined in [48], since the currents in the MFT of the 1:1-DCX are quasi-sinusoidal (also see **Fig. 2**), the MCT can be operated in a series resonant circuit that is supplied by a power amplifier to effectively emulate power operation. Furthermore, the large-signal validation is done with similar open-circuit primary voltage and short-circuit secondary current as for the ACT [48]. Due to test setup limitations, these are below nominal yet high enough to give sufficient confirmation of operation. Therefore, we use an AE Techron 7224 power amplifier and a series resonant capacitor to supply the MCT. The resonant capacitor C_r is realized as a high-frequency polypropylene capacitor bank (MMKP B32643B) and the series resonance frequency is set to $f_s = 39.6\,\mathrm{kHz}$ for short-circuit and $f_s = 41.5\,\mathrm{kHz}$ for open-circuit tests. The transformer currents are measured with Pearson 110A current probes and a LeCroy HDO4054A 12-bit oscilloscope. The current measurement is subject to a total uncertainty of $+2\,\%\ /\ -1\,\%$.

Fig. 16(a) shows the result of the test with a secondary-side short-circuit, which reveals a secondary-side rms current of $19.1\,\mathrm{A}$ for a primary-side rms current of $19.7\,\mathrm{A}$. This result agrees well with the expected secondary-side current of $19.3\,\mathrm{A}$ (for $k = 0.98$ as obtained from the impedance analyzer measurements described above, cf. **Tab. VIII**).

A second test with open secondary-side winding characterizes the self inductance of the MCT. **Fig. 16(b)** presents the measurement results, with a primary-side rms voltage of $2.01\,\mathrm{kV}$, a primary-side rms current of $7.2\,\mathrm{A}$, and a phase shift of 90°. This corresponds to a magnetizing inductance of $1.08\,\mathrm{mH}$, again corroborating the impedance analyzer measurement, see **Tab. VIII**.

C. Loss Measurements

1) Winding Losses: We validate the winding loss calculations by measuring the coils' AC resistances. Due to the low expected total AC resistance of the windings (approx. $30\,\mathrm{m\Omega}$), we employ the transient calorimetric method presented in [48]: the winding temperatures are measured with several NTC sensors (PS104J2 thermistors) placed in the winding package at the three positions marked with $T_{\{1,2,3\}}$ in **Fig. 8(b)**. In a first calibration step, the sensors' temperature responses to accurately measurable DC losses injected into the windings are measured. In a second step,

This article has been accepted for publication in IEEE Journal of Emerging and Selected Topics in Power Electronics. This is the author's version which has not been fully edited and content may change prior to final publication. Citation information: DOI 10.1109/JESTPE.2021.3123793

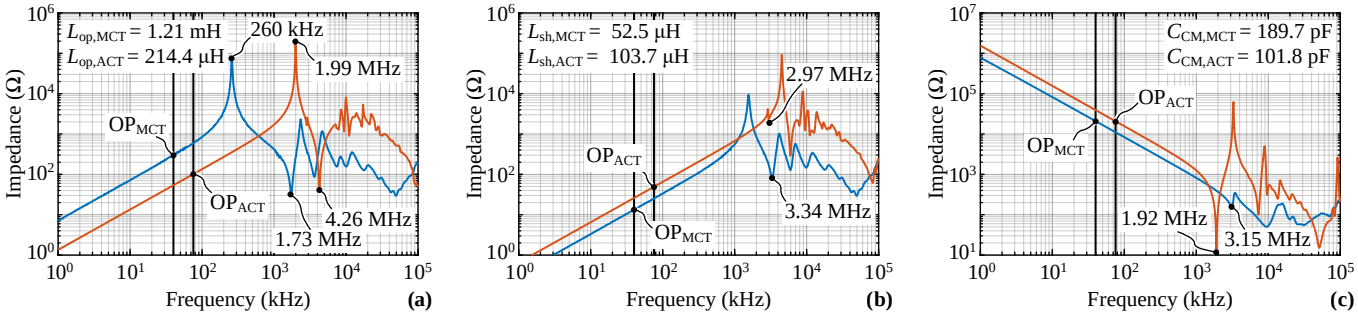

Fig. 15. Measured frequency characteristics of selected impedances of the transformers (MCT in blue; for reference, corresponding data for the ACT (w/o shielding) from [48] is shown in red): **(a)** primary-side impedance for open secondary-side winding; **(b)** primary-side impedance for shorted secondary-side winding; **(c)** CM impedance between shorted primary-side and shorted secondary-side windings. The impedance values corresponding to the operating frequencies (40.0 kHz for the MCT, 77.4 kHz for the ACT) are marked (OP).

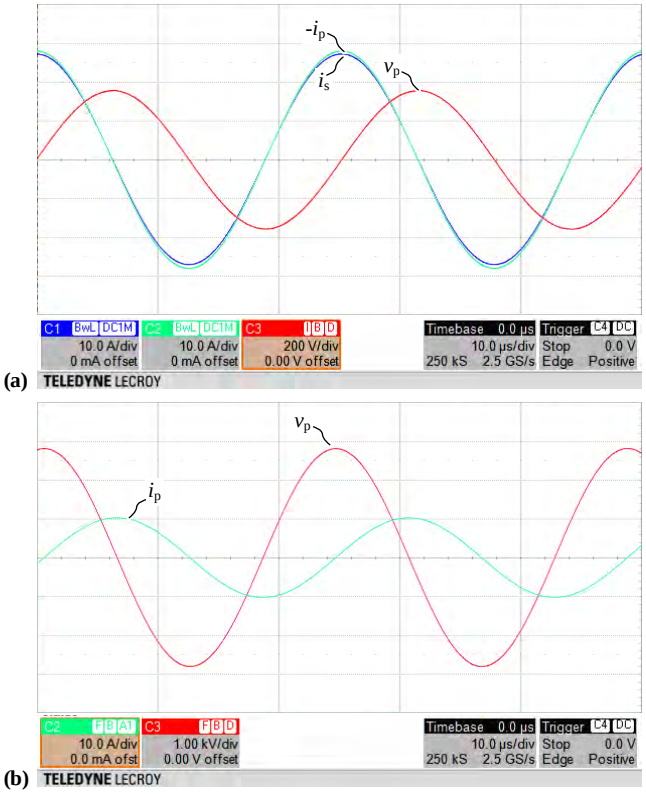

Fig. 16. Large-signal voltage and current waveforms of the MCT measured in series resonant operation. **(a)** Secondary-side short-circuit (rms values): primary-side current is 19.7 A, primary-side voltage is 0.25 kV, secondary-side current is 19.1 A, and resonance frequency is 39.6 kHz. **(b)** Secondary-side open-circuit (rms values): primary-side current is 7.2 A, primary-side voltage is 2.01 kV, and resonance frequency is 41.5 kHz.

the transformer is operated in AC series resonance (see **Section IV-B**) and the corresponding temperature measurements are recorded and translated into losses using the calibration data. Due to the high coupling of the MCT ($k = 0.98$) and as it corresponds to the relevant operation mode of the DCX, the experiments are done for the case of a short-circuited secondary-side winding only. The total AC resistance seen from the primary-side is finally extracted from the measured losses and the measured AC current.

TABLE IX. AC short-circuit resistance of the MCT windings obtained from transient calorimetric measurements at 39.6 kHz and comparison with value obtained from a 3D-FEM simulation.

Sensor	ΔT (°C)	P (W)	I_p (A)	I_s (A)	R_{AC} (mΩ)	$R_{AC,FEM}$ (mΩ)
Short-circuit						
T1	2.8	15.8			33.4	
T2	2.4	14.6	21.8	21.1	30.8	26.8 (18%)
T3	2.4	14.4			30.5	

Tab. IX lists the results. Averaging the values obtained based on the three different temperature sensors ($R_{AC,avg} = 31.6$ mΩ), the measured AC resistance is about 18 % higher than the result obtained from 3D-FEM simulations, i.e., in good agreement. Based on the measured AC resistance the nominal losses in the windings are computed as 105 W (at 130 °C).

2) Core Losses: During the optimization, core losses were calculated with the iGSE using manufacturer data (Steinmetz parameters for sinusoidal excitation) and analytically calculated flux densities. The accuracy of this approach mainly depends on the accuracy of the Steinmetz parameters. Therefore, the core loss characteristics of the material considered for the prototype (Ferroxcube 3C94, [93]) has been measured with sinusoidal excitation in a series resonance setup (open-circuit). A sample of two U126/72/20 core halves (without air gap) is placed in a temperature-controlled chamber and equipped with an excitation winding with a series capacitor (to compensate the reactive power) and a sense winding to measure to flux in the core (see **Fig. 17(a)**).

Fig. 17(b)-(c) present the measured loss density characteristics and **Tab. X** compares the core losses calculated with the measured loss map and 3D-FEM simulations of the actual flux density in the core of the prototype against the approach used in the optimization (based on analytical calculation of the flux density and datasheet-based Steinmetz parameters). The minor deviation of less than 10 % justifies using the datasheet-based loss map.

This article has been accepted for publication in IEEE Journal of Emerging and Selected Topics in Power Electronics. This is the author's version which has not been fully edited and content may change prior to final publication. Citation information: DOI 10.1109/JESTPE.2021.3123793

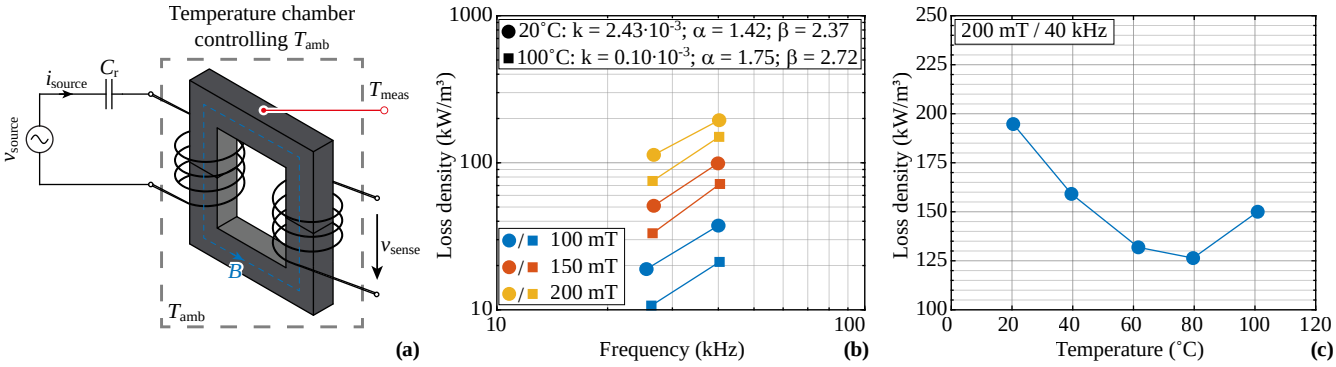

Fig. 17. **(a)** Schematic of the employed setup to extract the loss map of the MnZn ferrite material Ferroxcube 3C94. Loss density: **(b)** vs. frequency for various peak flux densities; **(c)** vs. temperature for the operating parameters of 200 mT / 40 kHz.

TABLE X. Comparison of core losses obtained from experiments (measured Steinmetz parameters and magnetic flux from 3D-FEM simulation) against the analytical results from the optimization obtained from analytical calculations using datasheet-based Steinmetz parameters of the considered ferrite material (3C94, [93]). Both methods use the iGSE equation.

Param.	Analyt.	Meas.	Deviation
P_{core}	363.5 W	328.4 W	9.6 %

D. Thermal Tests

To verify the thermal feasibility of the MCT, a heat run at the nominal operating point with active cooling (4×12 W) is carried out. We emulate these operating conditions using two independent DC circuits, cf. **Fig. 18(a)**. A DC current source is used to impress the nominal winding losses in the series connected windings, whereby the experimentally obtained ratio of AC to DC resistances ($R_{AC}/R_{DC} = 1.68$ @ 30 °C) is considered to achieve accurate results. To emulate the core losses, we utilize the electrical conductivity of the bulk ferrite, i.e., we treat the cores as electrical conductors [94], [95]. A closed circuit is formed by appropriately connecting the cores in series and in parallel with conductive silver glue (MG Chemicals 8331) and thin copper sheets as shown in **Figs. 18(b)–(c)**. Note that the equivalent center limb resistance ($R_{limb,c}$, cf. **Figs. 18(b)**) will not see the current flow and effectively can be modeled as an open-circuit. This leads to inhomogeneous distribution of losses within the core volume, and therefore represents the thermal worst-case for the core. Because of the strong inverse dependency of the ferrite electrical resistivity on temperature, the second DC source injecting the core losses operates in a controlled constant-power mode. This is a straightforward approach to test the thermal behavior of the transformer, because only DC power sources and relatively low voltages are required.

Fig. 19 shows the evolution of measured temperatures during the heat run and thermal images of the prototype taken after reaching the thermal steady-state under nominal operating conditions. Note that the losses injected into the windings are increased by 15 W to account for the dielectric losses (note that whereas during the optimization a value of 40 W has been used based on [6] (approx. 10% of

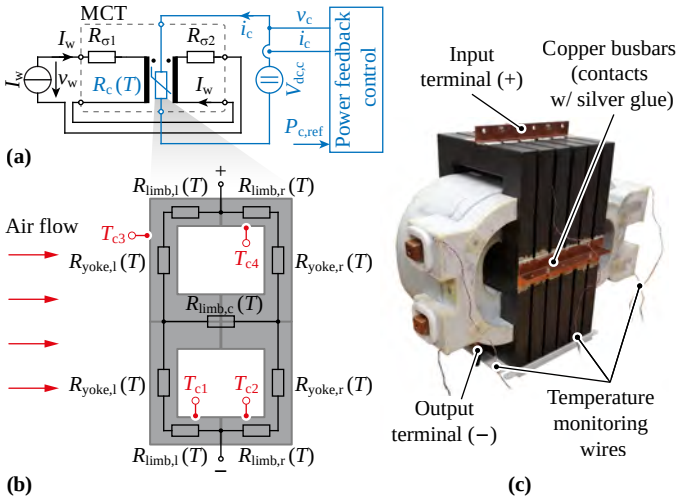

Fig. 18. DC-source based injection of winding and core losses for thermal verification. **(a)** Schematic showing the DC current source that impresses a DC current in the windings and the closed-loop controlled DC voltage source that impresses constant core losses. **(b)** Representative electrical network of stacked cores using a simplified model; note that the DC resistance of the ferrite is strongly temperature-dependent. For reference, the placement of PS104J2 NTC thermistors, $T_{c1...c4}$, in the core is shown. **(c)** Photo of the realized electrical connections of all the cores with the use of a conductive silver glue and copper busbars.

total losses), we measure much lower dielectric losses in the realized prototype, see **Section V-A**. At an ambient temperature of 25 °C, the maximum temperature measured with NTC sensors is 54 °C for the core and 56 °C for the windings, see **Fig. 19(a)**, whereas the surface hotspot registered with a FLIR camera reaches 70 °C on the core, cf. ① in **Fig. 19(b)**. The second image ② in **Fig. 19(b)** shows that the surface of the core which is directly exposed to the airflow has a lower surface hotspot temperature of less than 40 °C. **Fig. 19(c)** shows the change of the electrical resistances of the windings and of the ferrite cores during the test. The change of winding resistance allows to estimate the average temperature of the winding based on the copper properties as 63 °C. This leaves a margin of over 60 °C to $T_{max,w} = 130$°C (polyamide insulation). Similarly, the core has a temperature rise reserve of $\Delta T = 30$ °C, as the max-

This article has been accepted for publication in IEEE Journal of Emerging and Selected Topics in Power Electronics. This is the author's version which has not been fully edited and content may change prior to final publication. Citation information: DOI 10.1109/JESTPE.2021.3123793

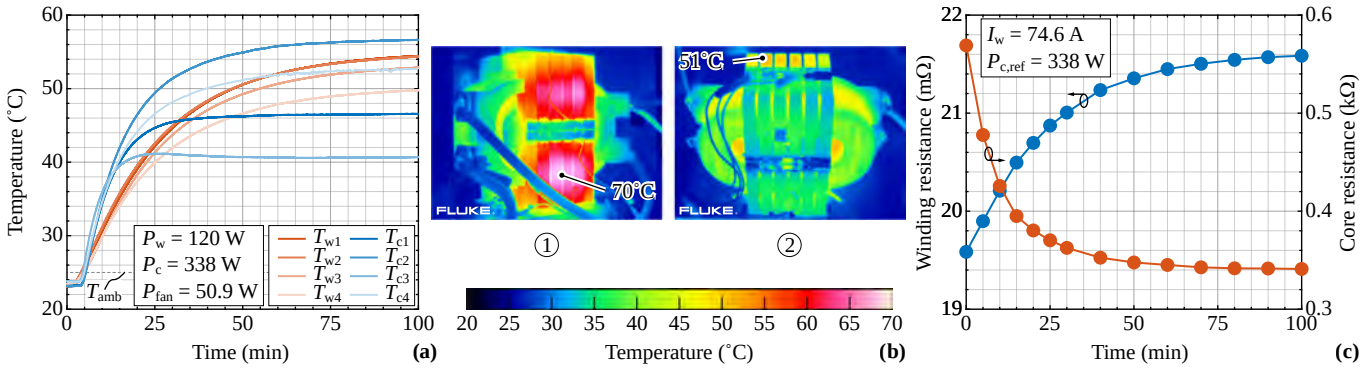

Fig. 19. **(a)** Temperatures measured with eight PS104J2 NTC thermistors ($T_{w1...w4}$ placed in the winding package and $T_{c1...c4}$ in the core) for a nominal load step with nominal cooling. **(b)** Corresponding thermal images with labeled hotspots of the MCT: ① front-side in the steady-state, ② back-side shortly after switching off the sources and cooling, and after removal of the enclosure with fans. **(c)** Measured change of winding and ferrite core DC resistance due to the temperature change; note the negative temperature coefficient of the ferrite DC resistance.

imum temperature of the core is defined as $T_{max,c} = 100°C$ due to the increased losses beyond that value. These margins would allow operation at ambient temperatures of up to 55 °C and the low thermal stress can be explained by the targeted high efficiency ($\geq 99\,\%$) of the DCX.

Furthermore, the thermal coupling between the winding package and the core is found to be very low. We inject nominal losses in one of the two and measure the temperature rise of the second. The experiments reveal that when the core is under load the average temperature rise of the winding package is only about 6 °C. Similarly, fully loaded windings yield a rise of the core temperature of only about 1 °C. This indicates that the MCT may have a very good overload capability, as thus increased winding losses will not give rise to a significant additional temperature increase of the core (which is closer to the temperature limit under nominal conditions). For that reason the overloading capabilities of both MCT and ACT are investigated in **Section V**.

Note that despite the overload capability, passive cooling of the MCT would not be feasible even for partial load due to relatively high losses in the core. In contrast, the ACT can operate with natural convection cooling up to 70 % of the rated power [48].

E. Insulation and Voltage Withstand Tests

To test the insulation of the transformer, first, the DC insulation resistance between primary and secondary side, i.e., the common-mode insulation, is measured with an insulation tester (Megger MIT410, DC test voltage of 1.1 kV). The measured insulation resistance is greater than 30 GΩ, which corresponds to a leakage current of less than 235 nA for a voltage of 7 kV. This insulation resistance is more than a hundred times higher than the specified minimum values [96], [97]. Additionally, the same insulation has been successfully tested at higher voltages, with a Schleich GLP2 voltage tester (for 1 min each): +9.6 kV (DC), −9.6 kV (DC), and 6.36 kV (rms) at $f = 50$ Hz. In summary, those tests indicate that the realized prototype withstands the rated insulation voltage.

F. Magnetic Stray Fields

In order to verify the levels of the magnetic field computed for the nominal operating point and presented in **Section III-B**, the magnetic stray flux densities are measured in the vicinity of the MCT using the field probe and setup presented in [48]. In a first step, the magnetic flux densities are computed with 3-D FEM simulations and normalized results (to 1 A rms) for open-circuit and short-circuit operation are presented in **Figs. 20(a)–(b)**, respectively. The simulations confirm that the highest values of magnetic field are in the plane of the air gap. Therefore the magnetic stray flux densities are measured in this plane and along the symmetry plane given by the x- and z-axis (see **Figs. 20(a)–(b)**). Furthermore, in each axis 9 points are selected for the validation.

During the tests, the MCT is operated in a series resonant circuit with a primary-side rms current of 1 A for open-circuit and 4 A for short-circuit at a frequency of 40 kHz. **Figs. 20(c)–(d)** present a comparison of normalized (to a current of 1 A) simulated and measured results. The average of the absolute value of the relative deviation between the simulated and the measured results is 10.6 % for an open secondary-side winding. The deviation increases to 32.8 % for x-axis and to 55 % for z-axis in case of shorted secondary-side as the expected flux densities are low and close to the lower end of the field probe's measurement range. Moreover, it was found that measurements in the range of several µT are challenging due to the residual magnetic fields generated by passive components of the circuits such as the cabling. In order to measure the fields for the case of secondary-side short-circuit with better accuracy, a higher measurement current could be used or alternatively a probe with a higher sensitivity be built. Nevertheless, the obtained results provide sufficient validation of the 3D-FEM simulations for nominal operation of the MCT presented in **Section III-B**.

V. Experimental Comparison of ACT & MCT

The basic experimental characterizations of the MV/MF ACT and MCT prototypes shown in **Fig. 13** have been

This article has been accepted for publication in IEEE Journal of Emerging and Selected Topics in Power Electronics. This is the author's version which has not been fully edited and content may change prior to final publication. Citation information: DOI 10.1109/JESTPE.2021.3123793

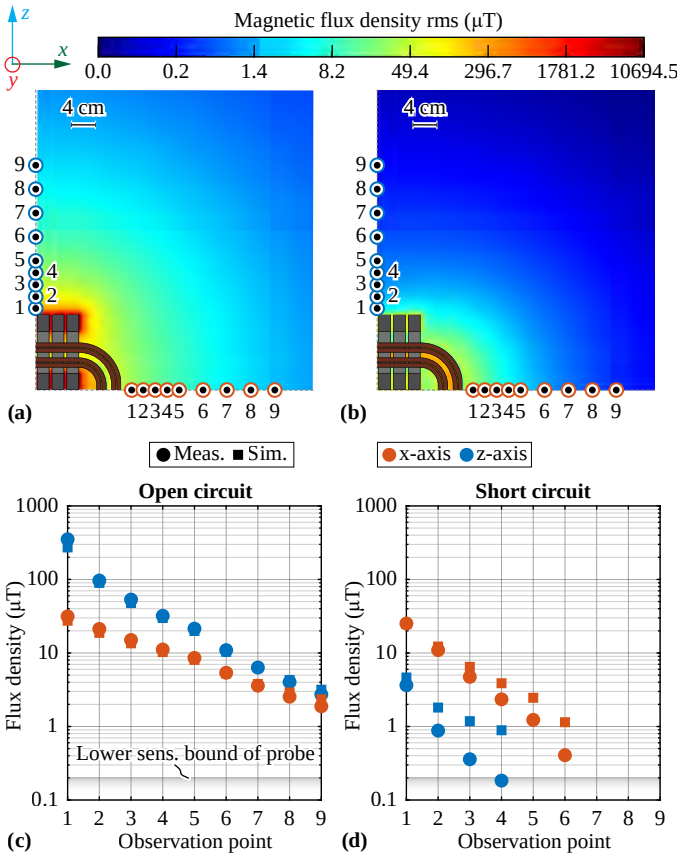

Fig. 20. Simulated rms values of the mag. flux densities in the plane of the air gap for secondary-side **(a)** open-circuit and **(b)** short-circuit. **(c)–(d)** Respective measured and simulated rms values of the magnetic flux densities at the observation points (normalized to a primary-side current of 1 A).

presented in [48] and in **Section IV**, respectively, and **Tab. VII** summarizes the key characteristics. This section extends the provided experimental analysis of the realized transformers by a detailed comparative experimental evaluation of dielectric losses and the overload capability.

A. Dielectric Losses

Dielectric losses can contribute a non-negligible share of total MFT losses in case of dry-type insulation systems [78]. Therefore, we provide an experimental verification of the corresponding assumptions made during the optimization. The dielectric response of the employed insulation materials is linear with the electric field in the range of practically relevant field strengths (at most some kV/mm). Therefore, the dielectric losses of the constituting materials can be measured with small-signal excitations [78], and 3-D FEM electric field simulations can be employed to compute the dielectric losses of the transformer assembly. For validation, we then provide also measurements of the dielectric responses of the entire transformer assemblies and compare them to the results obtained by the FEM-based calculation. For all dielectric response measurements, a setup consisting of a Novocontrol Broadband Dielectric Spectrometer with an Alpha-A High Performance Frequency Analyzer [98] is used.

TABLE XI. Measured dielectric properties of the materials employed in the MFT prototypes (valid for operating frequencies in the range of $40-80\,\mathrm{kHz}$, at 25°C and 45% relative humidity).

Material	**Diel. constant** ε_r	**Diss. factor** $\tan\delta$
Silicone	4.1	0.8 %
PC	2.7	0.3 %
Aramid polymer (Nomex 993)	3.2	1.9 %
PMMA	3.0	2.4 %

First, we measure the frequency-dependent dielectric responses of the insulation/construction materials employed in the ACT and MCT prototypes: silicone TC4605 HLV (dry-type insulation), polycarbonate (coil formers), aramid polymer Nomex (spacers and barriers), and PMMA (mechanical supports). **Fig. 21(a)** shows the measurement cell with an exemplary sample and **Fig. 21(b)** gives the results. Note that the samples have been stored under room conditions (22°C and 45 % relative humidity (RH)) before the measurements. **Tab. XI** summarizes the dissipation factors and the dielectric constants extracted for the considered frequency range $(40-80\,\mathrm{kHz})$. Using these parameters in a 3D-FEM simulation of the electric fields in the dielectric materials of the MCT and of the ACT yields the dielectric losses, CM capacitances and total dissipation factors given in **Tab. XII(a)**. Note that we consider two values for the dissipation factor of silicone (minimum and maximum) to account for environmental and temperature effects, which will be discussed shortly. The high-field region in the MCT (inter-winding space, cf. **Fig. 9(a)**) is mainly filled with dry-type insulation, thus the silicone accounts for up to 95 % of the MCT's total dielectric losses, leading to a worst-case total dissipation factor $\tan\delta_\mathrm{MCT}\approx 1.0\%$. On the other hand, as expected, the dielectric losses of the ACT can be neglected as $\tan\delta_\mathrm{ACT}\approx 0.1\%$. Lastly, the computation of the CM capacitances shows very good agreement with the small-signal impedance measurements presented earlier ($<9\,\%$, cf. **Fig. 15(c)**).

As the dielectric losses of the ACT can be neglected, only the dielectric response of the entire MCT is measured. **Fig. 21(c)** shows the measured dissipation factor of the MCT, which was stored at room conditions (22°C, 45 % RH) prior to the test. At $40\,\mathrm{kHz}$ we measure $\tan\delta_\mathrm{MCT}=5.6\%$, which is surprisingly high compared to the value computed by the 3D-FEM simulation ($\tan\delta_\mathrm{MCT}\approx 1.0\%$) using the dissipation factors measured for the individual material samples. Since the behavior of the silicone dominates $\tan\delta_\mathrm{MCT}$, we further investigate the influence of the initial environmental conditioning (namely the impact of water ingress into the polymer during storage) on the dissipation factor of the silicone.

Therefore, three silicone specimens of $1.2\,\mathrm{mm}$ thickness are prepared and conditioned in environments with different relative humidity after first exposing them for 4 hours to a temperature of 120°C in an atmosphere of dry air, which ensures equal initial conditions by erasing the effects of previous tests. Afterwards, the following conditioning procedures were applied:

This article has been accepted for publication in IEEE Journal of Emerging and Selected Topics in Power Electronics. This is the author's version which has not been fully edited and content may change prior to final publication. Citation information: DOI 10.1109/JESTPE.2021.3123793

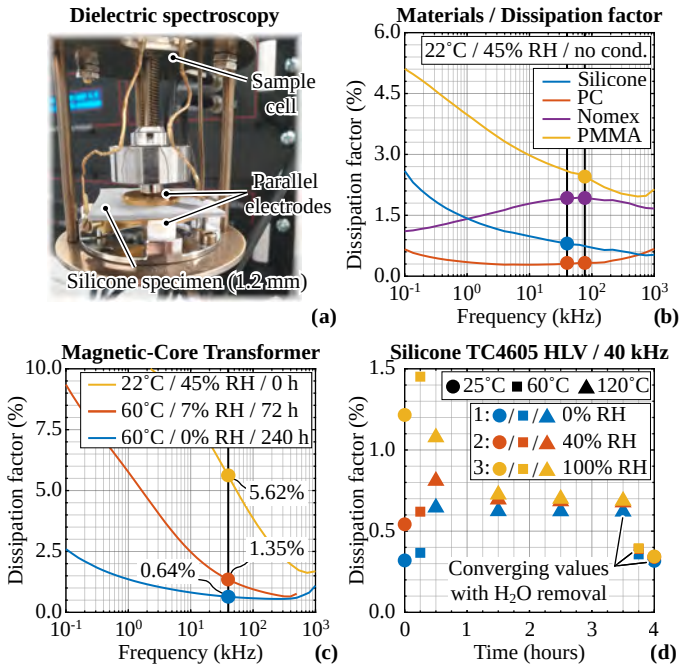

Fig. 21. **(a)** Photo of the dielectric spectrometry setup with an exemplary material specimen (silicone, thickness of 1.2 mm) placed in the sample cell. **(b)** Frequency characteristic of the dissipation factors of the construction/dielectric materials used for the realization of transformers (at 22°C, 45% RH, w/o conditioning). **(c)** Measured dissipation factor of the entire MCT stored in different conditions prior to the measurement: 22°C, 45% RH (w/o conditioning); 60°C, 7% ambient RH (cond. 72 hours); 60°C, 0% RH (cond. 240 hours). **(d)** Time evolution of the measured dissipation factors of three silicone specimens stored in different environments before the test under the indicated heating protocol (25°C → 60°C → 120°C (3 hours) → 60°C → 25°C).

- Sample 1: stored for 20 hours at 120°C and 0% RH (in N_2 atmosphere).
- Sample 2: stored for 2 weeks at 25°C and 40% RH.
- Sample 3: stored for 2 weeks at 25°C and 100% RH (non-condensing).

Then, the dissipation factors of all samples are measured in the same chamber during a heating cycle consisting of a temperature ramp from 25°C to 120°C, 3 hours conditioning at 120°C, and a ramp down back to 25°C. The results are presented in **Fig. 21(d)**. It can be seen that the initial dissipation factor depends strongly on the initial relative humidity of the sample and ranges from $0.3\,\%$ (sample 1) to $1.2\,\%$ (sample 3). During the first part of the heating sequence, two opposing effects are active simultaneously: the increased sample temperature causes an increase of the dissipation factor for a given water content [99], while the initiated removal of moisture decreases it. The measurements confirm that in all cases the exposure to a higher temperature over some hours removes moisture from the samples by thermal diffusion. Indeed, towards the end of the heating sequence, the dissipation factors of all samples converge to approximately $0.3\,\%$. This equals the initial value for sample 1, which suggests almost complete removal of any residual moisture.

In light of these results, the MCT was conditioned by placing it in an oven (natural convection) for a total of 72 hours. The temperature was regulated to 60°C at RH of $7\,\%$ (which corresponds to RH of $45\,\%$ at room temperature). **Fig. 21(c)** shows that the dissipation factor of the MCT is still relatively high compared to the computed value ($1.4\,\%$ vs. $1.0\,\%$). To further reduce the moisture content of the insulation, we placed the MCT in the oven at 60°C with a dry purge airflow (absolute and relative humidity close to 0%) for a total of 240 hours. As expected, the measured value of $\tan\delta_{\mathrm{MCT}} = 0.64\%$ (cf. **Tab. XII(b)**) matches the result obtained above for the silicone samples at 60°C towards the end of the heating sequence[1] ($\tan\delta_{\mathrm{silicone}} \approx 0.4\%$, cf. **Fig. 21(d)**).

These results highlight the important impact of the initial environmental conditioning on the dissipation factor of dry-type MFTs with silicone insulation, and hence on the dielectric losses. Depending on the initial moisture content of the silicone, the dielectric losses can initially be several times higher than what would be expected from values obtained from a "dry" transformer (e.g., after operating for several hours in thermal steady state). This worst-case scenario should be considered during the design, e.g., by taking into account a range (min./max.) for the dissipation factor instead of a single value (see **Tab. XII(a)**).

TABLE XII. FEM-simulated dielectric losses, CM capacitances and dissipation factors of MFTs. Comparison with measurement results obtained with dielectric spectrometer.

(a) Sim. param.	**MCT**		**ACT**
	Min.	Max.	
Silicone tanδ	0.4 %	1.2 %	
Losses			
Silicone	3.61 W	10.83 W	–
Coil formers (PC)	0.40 W	0.40 W	0.44 W
Spacers / barriers (Nomex)	0.02 W	0.02 W	0.77 W
Supports (PMMA)	–	–	0.69 W
Total	4.0 W	11.2 W	1.9 W
CM capacitance	187.6 pF		111.2 pF
Dissipation factor	0.35 %	0.97 %	0.14 %
(b) Meas. param.			
CM capacitance	161.1 pF		106.8 pF
Dissipation factor	0.64 %	5.62 %	–

B. *Long-Term Overload Capability*

The heat runs with losses corresponding to the nominal output power (cf. **Section IV-D** and [48]) reveal that the steady-state temperatures of the MCT and the ACT leave significant margins with respect to the maximum allowable values. In case of the MCT, this can be explained by the fact that the loss penalty factors included in the design (for winding and core losses) were too conservative. Therefore, the

[1]Considering that $95\,\%$ of the total dielectric losses in the MCT occur in the silicone.

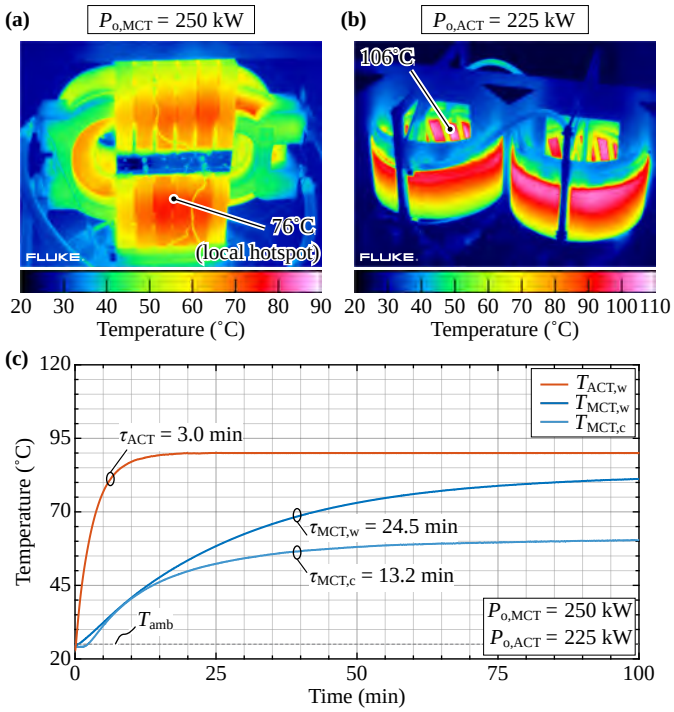

Fig. 22. Thermal images of the transformers in the thermal steady-state at maximum overload with (surface) hotspot temperatures indicated: **(a)** MCT with losses corresponding to operation at 250 kW, **(a)** ACT with losses corresponding to operation at 225 kW. **(c)** Maximum temperatures measured with NTC thermistors ($T_{ACT,w}$: windings of the ACT; $T_{MCT,w}$ and $T_{MCT,c}$: windings and core of the MCT, respectively) during the corresponding overload heat runs.

realized cooling system enables operation of the transformer at lower temperatures than designed for. Furthermore, the airflow at the air inlet of the MCT enclosure was measured with an airflow meter. Due to very turbulent nature of the air in the enclosure, locally the airflow speed reaches up to $9\,\mathrm{m/s}$, which is almost twice the assumed value of $5\,\mathrm{m/s}$, further improving the performance of the cooling system.

Similarly, the simplified thermal model of the ACT is based on a surface related-loss density of $p_{v,max} = 0.25$ W/cm^2), an assumption which has been found to be too conservative, too, because [48] demonstrates that $p_{v,max} = 0.30$ W/cm^2 is achievable. Additionally, the analysis of the temperature gradient along the circumference of the coils shows that due to the mismatch of the fan and coil diameters (with fans being smaller, cf. **Fig. 10(a)**), the outer parts of the windings are not situated in the direct airflow, leading to local hot-spots. For this reason, we place air ducts to guide the airflow along the whole circumference of the coils, thus potentially unlocking operation with even higher surface-related loss densities.

To evaluate the overload capability, we carry out heat runs with losses that correspond to operation at higher-than-nominal power. The maximum temperatures that must not be exceeded once steady-state is attained are defined as $T_{hs,c} = 100$°C (hotspot in the core), $T_{hs,w} = 105$°C (hotspot in the winding), $T_{avg,w} = 95$°C (maximum average winding temp.) for the ambient temperature of 25°C. **Figs. 22(a)–(b)** show the thermal images of the transformers operated with losses that correspond to the maximum possible overload power and **Fig. 22(c)** presents the evolution of maximum measured temperature waveforms during the corresponding heat runs. The results show that the MCT can be operated with a power transfer of up to $250\,\mathrm{kW}$ ($P_w = 249$W, $P_c = 340$W, $P_{fan} = 48$W), whereas the ACT can reach $225\,\mathrm{kW}$ ($P_w = 1281$W, $P_{fan} = 48$W). The average winding temperatures are 94.2°C and 90.3°C for the MCT and ACT, respectively (at 25°C ambient). Furthermore, in the overload test the ACT achieves a surface-related winding loss density of $p_{v,max} = 0.47$ W/cm^2. Note that for long-term overload operation in industrial environments, it would be preferable to use litz wires of higher temperature class than the ones used in the prototypes (V155).

Finally, the thermal time constants can be extracted from **Fig. 22(c)** as $13.2\,\mathrm{min}$ for the core and $24.5\,\mathrm{min}$ for the MCT's winding package, in contrast to $3.0\,\mathrm{min}$ for the ACT. With this, it can be concluded that the MCT's short-term overload capability ($< 10\,\mathrm{min}$) is significantly higher than that of the ACT because of the approximately $8\times$ longer thermal time constant of the windings. Note that the thermal coupling from windings to the core is relatively weak, therefore the time constant of the core is unimportant for this consideration.

VI. System-Level 1:1-DCX Performance Evaluation

The initial Pareto optimization and the extensive experimental analysis of full-scale ACT and and MCT prototypes provide a solid basis for a concluding quantitative system-level performance comparison of the ACT- and MCT-based 1:1-DCX, and finally a qualitative application-oriented evaluation.

A. System-Level Performance of ACT- and MCT-DCX

The actually realized transformer prototypes and the corresponding 1:1-DCXs are indicated with a ☆ in the performance spaces obtained from the optimization in **Fig. 7**. **Fig. 23** shows the breakdowns of masses, volumes, and losses of the components employed in the two 1:1-DCX designs. The values for the two transformers and for the resonant capacitor banks are measured as described above, whereas the remaining data follows from the modeling used for the Pareto optimization (see **Section II**); note that the calculation of the MOSFET masses, volumes and losses relies on experimental data from [61], [62]. Therefore, all important contributions to mass, volume, and losses of the two systems are backed by experimental results, which enables a realistic comparison.

The mass breakdown (see **Fig. 23(a)**) shows that the mass of the MCT accounts for about $84\,\%$ of the total converter's mass with the core alone contributing $45\,\%$. In addition, also the dry-type insulation increases the overall weight considerably. Interestingly, the weights of windings and coil formers are very similar for both transformers. Due to the low copper mass of the ACT, the realization of mechanical parts such as coil formers, supports, and fixtures becomes important, as they account for more than $55\,\%$ of the ACT's total mass. On the other hand, the capacitor bank for the

This article has been accepted for publication in IEEE Journal of Emerging and Selected Topics in Power Electronics. This is the author's version which has not been fully edited and content may change prior to final publication. Citation information: DOI 10.1109/JESTPE.2021.3123793

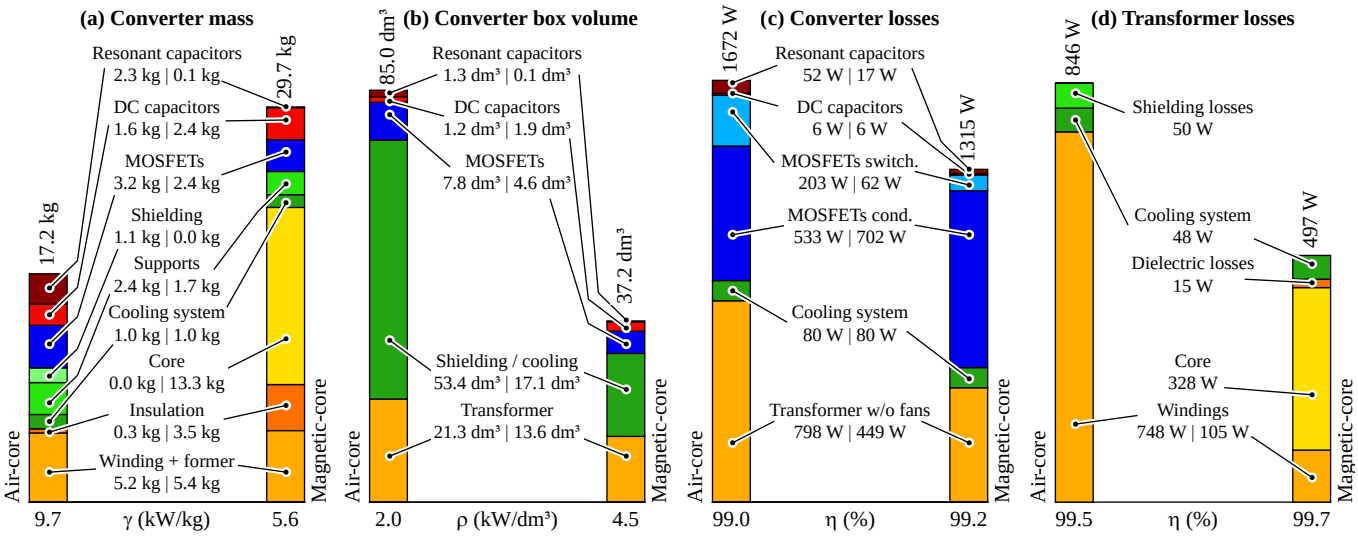

Fig. 23. Breakdown of the **(a)** masses, **(b)** volumes, **(c)** losses of the components employed in the ACT-based and MCT-based 166 kW / 7 kV 1:1-DCX designs. **(d)** Measured transformers losses including losses for the cooling system.

MCT-DCX can be realized as a PCB with C0G ceramic capacitors of almost negligible mass, which represents a clear advantage over the ACT-DCX that requires high-power capacitors with a dedicated cooling system consisting of heatsinks and fans, which ultimately contributes more than 14 % of the converter's total mass. Overall, the ACT-DCX features a gravimetric power density of $\gamma = 9.7\,\mathrm{kW/kg}$, whereas the MCT-DCX achieves $\gamma = 5.6\,\mathrm{kW/kg}$.

Not considering the ACT's shielding, its boxed volume is still 56 % larger than the MCT's, see **Fig. 23(b)**. Nevertheless, the ACT itself achieves a rather high volumetric power density of $7.8\,\mathrm{kW/dm^3}$. However, the overall converter volume is dominated by the volume of the shielding enclosure around the ACT. Therefore, the MCT-DCX is significantly more compact and features a 2.2× higher volumetric power density. Note that the shielding enclosure of the ACT could be much more compact, however, with a trade-off of increased losses (in the built prototype the objective was to obtain marginal losses in the shielding)[2].

The breakdown of the converters' losses at nominal power (see. **Fig. 23(c)**) shows that the total semiconductor losses are almost equal for both solutions (764 W for the MCT-DCX vs. 736 W for the ACT-DCX) even though the switched/conducted currents and the switching frequencies are higher in the ACT-DCX. It is important to highlight that this is achieved by employing more chip area in the ACT-DCX, i.e., a total of 6 paralleled dies (3 packages) are used compared to only 4 parallel dies (2 packages) in case of the MCT-DCX. Therefore, the realization of the half-bridges of the ACT-DCX switching stages is more complex (gate driving circuitry) and especially significantly more expensive, in addition to requiring a bulkier cooling system that is reflected in the increased mass and volume, cf. **Fig. 23(a)–(b)**. On the system-level, with 99.2 % efficiency the MCT-DCX achieves a slightly higher DC-DC efficiency at nominal load than the ACT-DCX (99.0 %); the quite different efficiency characteristics at partial-load operation will be discussed below.

Fig. 23(d) provides detailed insight into the transformer loss components. The majority of MCT's losses are core losses (about 73 %). This is a characteristic of the weight-optimized design, as it is much easier to extract the heat from the stacked cores with air channels in between compared to extracting losses from the potted winding. Furthermore, relatively high core losses are a consequence of selecting a design with rather high magnetic flux densities, which reduces the necessary core cross section and thus reduces its mass. The ACT incurs a 0.2 % efficiency penalty compared to the MCT, which is mainly attributed to the higher-than-necessary winding losses: due to imperfect twisting, the litz wire used in the prototype has been measured to cause up to 30 % higher losses [48]. With a correctly manufactured litz wire, the efficiency is expected to increase by 0.1 %, bringing it close to that of the MCT.

For a comprehensive evaluation of the efficiency, **Fig. 24** shows measured (stars) and simulated (circles for MFTs and squares for 1:1-DCXs) efficiency curves for the ACT and the MCT as well as the corresponding DCX systems. Note that the ACT can operate with passive cooling (fans not activated and corresponding losses not considered) up to about 70 % of the rated power. The ACT's efficiency curve is rather flat and shows a very high partial-load efficiency, i.e. $\eta > 99.4\,\%$ applies for a very wide range of the output power of $P_\mathrm{o} \in [15\%, 100\%]P_\mathrm{N}$. In contrast, the MCT features comparatively low partial-load efficiency due to relatively high load-independent core losses. Thus, for the realized prototypes, the ACT outperforms the MCT in terms of efficiency for output power levels of up to $P_\mathrm{o} \approx 70\%P_\mathrm{N}$.

With regard to the overall 1:1-DCX systems, both efficiency curves are relatively flat for loads between 35 % and 100 % of the nominal power. The MCT-DCX attains a very high efficiency (close to 99.2 %) even up to $110\%P_\mathrm{N}$. Conversely, the ACT-DCX achieves slightly higher part-load efficiency for loads $< 40\%P_\mathrm{N}$ due to the aforementioned ex-

[2]Furthermore, no shielding is considered for the MCT.

This article has been accepted for publication in IEEE Journal of Emerging and Selected Topics in Power Electronics. This is the author's version which has not been fully edited and content may change prior to final publication. Citation information: DOI 10.1109/JESTPE.2021.3123793

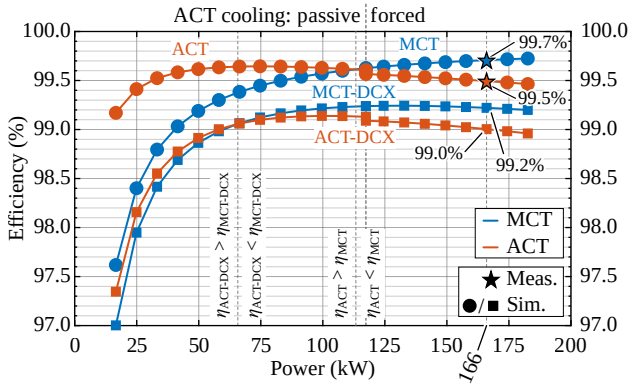

Fig. 24. Measured (★) and simulated (● / ■) efficiencies of the transformers and the complete 1:1-DCXs (MCT-based in blue, ACT-based in red).

ceptional partial-load characteristic of the ACT and in spite of high magnetizing current which causes load-independent switching losses in MOSFETs. From the similarity of the system-level efficiency curves at low loads, we conclude that the impact of the magnetizing current losses in the ACT-DCX is comparable to the transformer's core losses in the MCT-DCX. Finally, at the rated power of $P_\mathrm{N} = 166\,\mathrm{kW}$, the transformer efficiencies are $99.7\,\%$ and $99.5\,\%$ for the MCT and ACT, respectively, whereas the DC-DC efficiencies reach $99.2\,\%$ for the MCT-DCX and $99.0\,\%$ for the ACT-DCX.

B. Application-Oriented Evaluation

From the quantitative results presented above, we conclude that ACTs represent a promising alternative to dry-type MCTs for isolated DC-DC converters, in particular for 1:1-DCX applications, where similar efficiency characteristics can be achieved. However, both concepts show distinct strengths and weaknesses. To aid in selecting the concept most suitable for a specific application, we provide a qualitative discussion of the key distinctive features in the following:

- *Lightweight* - ACTs can achieve several times higher gravimetric power density compared to MCTs. However, on the system-level this advantage reduces to about $2\times$ higher gravimetric power density of the ACT-DCX compared to the MCT-DCX.
- *Compactness* - Due to lack of guidance for the magnetic flux and the resulting shielding requirements, the volume of an ACT is relatively high. ACTs thus achieve significantly lower volumetric power density. Consequently, MCT-based systems are more favorable for compact solutions.
- *Linearity* - ACTs are perfectly linear and, therefore, can withstand significant temporary overcurrents or overvoltages without changing their properties. Because of the nonlinear behavior (e.g., saturation) of the magnetic cores, this is not the case for MCTs.
- *Temperature* - The operating temperature of ACTs is not limited by the Curie temperature of a magnetic core material. Therefore, ACTs are well suited for high-temperature environments provided that high temperature grade litz wires are used. Furthermore, due to simple construction, thermal management is straightforward compared to MCTs with dry-type insulation systems.
- *Overload capabilities* - Due to the linearity and high-temperature capability of an ACT, and owing to the large thermal time constant of the MCT, both solutions offer good long-term overload capabilities.
- *Stray field / shielding* - The medium-frequency magnetic stray field emitted by MFTs is not negligible and should be shielded in order to avoid eddy current losses in nearby metallic conductors and/or electromagnetic interference issues. However, the magnetic stray fields in the vicinity of an MCT are typically lower and decay faster with distance. Hence, ensuring a relatively small distance to other equipment or persons is usually sufficient. In contrast, ACTs typically require explicit shielding. If this is not anyway provided from the application's assembly situation (e.g., cabinet), a low-loss and lightweight conductive shielding can be implemented.
- *Insulation coordination* - ACTs employ air as insulation medium. The required clearance and creepage distances can be tailored, even for a finished design, by inserting appropriate barrier elements between the coils. This is advantageous, e.g., for input-series output-parallel (ISOP) arrangements of DCX cells as the transformers are experiencing different CM voltages in such converter structures, or for airborne applications, where the insulation strength of air depends on altitude. In contrast, once the insulation system of an MCT has been defined, the insulation voltage rating cannot be changed anymore.
- *Dielectric losses* - Thanks to the employed air insulation, the dielectric losses of the ACT can be neglected. Conversely, the dielectric losses of dry-type MCTs with silicone insulation must be taken into account, and in particular the impact of initial environmental conditioning (relative humidity).
- *Construction* - Clearly, the construction of ACTs is relatively simple, as mainly structural elements to support the windings are needed. In contrast, dry-type MCTs require a controlled pressurized vacuum potting process to achieve a void-free insulation system.
- *Resonant capacitor bank* - Due to relatively high leakage inductances, an ACT requires low resonant capacitance values for a given operating frequency, which results in high resonant capacitor voltages. Therefore, high-power capacitor bank assemblies are necessary, which are bulky and generate significant losses (possibly requiring active cooling). On the other hand, for the MCTs, the capacitor bank for the considered 1:1-DCX could be realized with ceramic capacitors of negligible losses, mass and volume.
- *Semiconductors* - Owing to the higher operating frequency and rms currents (due to higher magnetizing current), an ACT-DCX requires more power semiconductor chip area per switch than an MCT-DCX, which results in higher converter cost and increased

realization complexity. Nevertheless, the high magnetizing currents of ACTs are advantageous for soft-switching applications.

VII. Conclusion

This paper quantifies the theoretical performance limits of a $166\,\mathrm{kW}$ / $7\,\mathrm{kV}$ air-core transformer (ACT) and magnetic-core transformer (MCT) for unity voltage conversion ratio (1:1-DC transformer, 1:1-DCX) application on both, the component (transformer) and on the system (DCX) level. The results of a multi-objective optimization show that ACTs can achieve several times higher gravimetric power densities compared to MCTs. Furthermore, on the system-level, ACT-based DCXs reach about two times higher gravimetric power density compared to MCT-based DCXs. However, ACTs typically require a shielding enclosure to limit magnetic stray fields, which increases the volume. Thus, only about half of an MCT's volumetric power density is achievable.

To validate the employed models and theoretical analysis, two medium-frequency transformers (MFTs) are selected for realization, each representing one of the concepts, i.e., ACT and MCT. The ACT consists of two sets of coaxially arranged solenoids, achieving a relatively high coupling factor (0.76) and it employs air as insulation and cooling medium. The MCT is a shell-type transformer consisting of an E-core with concentric windings encapsulated in silicone insulation (dry-type insulation system).

Both full-scale MFT prototypes are experimentally characterized in detail, facilitating a realistic comparative evaluation. MFTs feature a nominal insulation voltage of $10\,\mathrm{kV}$ with clearance and creepage distances realized according to IEC 62477. It has been shown that initial environmental conditioning of the MCT's dry-type silicone insulation has a significant influence on the dielectric losses. Depending on the state of the silicone (moist or dry), the dielectric losses can vary by more than a factor of three. Hence, in some dry-type MFTs the dielectric losses can account for up to $15\,\%$ of the total losses and must be considered in the design calculations. In contrast, there are no noteworthy dielectric losses in an ACT, thanks to the air insulation.

The measurements of the magnetic stray flux in the proximity of the MFTs confirm that shielding is required for the ACT prototype to conform with the ICNIRP (2010) exposure limits. This can be achieved with a lightweight, low-loss conductive shielding. On the other hand, the MCT prototype does not require additional shielding, as stray fields decay below the limits already geometrically relatively close to the MFT ($250\,\mathrm{mm}$), a distance which is a reasonable clearance to maintain in MV systems.

Conservative assumptions during the optimization and design phase enable significant overload capability of both prototypes, as winding and core temperatures in thermal steady-state with injected core and winding losses that correspond to the nominal operating point remain clearly below limiting values. Therefore, we carried out heat runs with losses that correspond to maximum thermally feasible power transfer. At room temperature, the MCT prototype can be operated with power transfer of up to $250\,\mathrm{kW}$, whereas the ACT prototype can reach $225\,\mathrm{kW}$.

The ACT prototype ($16.5\,\mathrm{kW/kg}$, $2.2\,\mathrm{kW/dm^3}$) achieves a measured full-load efficiency of $99.5\,\%$ at an operating frequency of $77.4\,\mathrm{kHz}$. The MCT prototype ($6.7\,\mathrm{kW/kg}$, $5.4\,\mathrm{kW/dm^3}$), operated at $40.0\,\mathrm{kHz}$, reaches a measured efficiency of $99.7\,\%$. Furthermore, the use of $10\,\mathrm{kV}$ SiC MOSFETs enables system-level efficiencies (calculated) for the ACT-DCX and the MCT-DCX of $99.0\,\%$ and $99.2\,\%$, respectively. Moreover, both DCXs are characterized by a flat efficiency curve, with the ACT-DCX's efficiency being slightly higher for loads $< 40\%$ of rated power, thanks to the ACT's low no-load losses. In contrast, for higher power levels, the MCT's relatively low winding losses enable higher efficiencies.

Finally, the presented application-oriented qualitative evaluation clarifies the strengths and weaknesses of the ACT- and MCT-based systems, and can aid in the selection of the most suitable concept for a given application.

Acknowledgements

The authors are very much indebted to the Swiss Centre for Competence in Energy Research on the Future Swiss Electrical Infrastructure (SCCER-FURIES) for the support of the research in the area of Solid-State Transformer technology at the ETH Zurich.

Furthermore, special thanks go to Dr. Sven Friedel from COMSOL Multiphysics GmbH for the technical support with FEM simulations. The dielectric spectroscopy of the materials used for construction of the transformers was carried out at Advanced Power Semiconductor Laboratory (APS) of ETH Zurich. Finally, the authors would like to gratefully extend their thanks to R. Goldhorn from TDK Europe GmbH for providing samples of MMKP capacitors.

References

[1] J. E. Huber and J. W. Kolar, "Applicability of Solid-State Transformers in Today's and Future Distribution Grids," *IEEE Trans. Smart Grid*, vol. 10, no. 1, pp. 317–326, 2019.

[2] T. Dragicevic, J. C. Vasquez, J. M. Guerrero *et al.*, "Advanced LVDC Electrical Power Architectures and Microgrids: A Step Toward a New Generation of Power Distribution Networks." *IEEE Electrific. Mag.*, vol. 2, no. 1, pp. 54–65, 2014.

[3] P. C. Kjaer, Y.-H. Chen, and C. G. Dincan, "DC Collection: Wind Power Plant with Medium Voltage DC Power Collection Network," presented at the ECPE Workshop Smart Transf. Traction Future Grid Appl., Zurich, Switzerland, 2016.

[4] S. Falcones, R. Ayyanar, and X. Mao, "A DC–DC Multiport-Converter-Based Solid-State Transformer Integrating Distributed Generation and Storage," *IEEE Trans. Power Electron.*, vol. 28, no. 5, pp. 2192–2203, 2013.

[5] B. Hafez, H. S. Krishnamoorthy, P. Enjeti *et al.*, "Medium Voltage Power Distribution Architecture with Medium Frequency Isolation Transformer for Data Centers," in *Proc. of the IEEE Appl. Power Electron. Conf. and Expo. (APEC)*, 2014.

[6] D. Rothmund, T. Guillod, D. Bortis *et al.*, "99 % Efficient 10 kV SiC-Based 7 kV/400 V DC-Transformer for Future Data Centers," *IEEE Trans. Emerg. Sel. Topics Power Electron.*, vol. 7, no. 2, pp. 753–767, 2019.

[7] S. Srdic and S. Lukic, "Toward Extreme Fast Charging: Challenges and Opportunities in Directly Connecting to Medium-Voltage Line," *IEEE Electrific. Mag.*, vol. 7, no. 1, pp. 22–31, 2019.

[8] H. Tu, H. Feng, S. Srdic *et al.*, "Extreme Fast Charging of Electric Vehicles: A Technology Overview," *IEEE Trans. Transport. Electrific.*, vol. 5, no. 4, pp. 861–878, 2019.

[9] S. Castellan, R. Menis, A. Tessarolo *et al.*, "Power Electronics for All-Electric Ships with MVDC Power Distribution System: An Overview," in *Proc. of the IEEE Int. Conf. on Ecological Vehicles and Renewable Energies (EVER)*, 2014.

[10] *ABB Marine & Ports*, "Onboard DC Grid – A System Platform at the Heart of Shipping 4.0," https://new.abb.com/marine/generations.

[11] G. Ulissi, S.-Y. Lee, and D. Dujic, "Solid-State Bus-Tie Switch for Shipboard Power Distribution Networks," *IEEE Trans. Transport. Electrific.*, vol. 6, no. 3, pp. 2332–7782, 2020.

[12] N. Madavan, "NASA Investments in Electric Propulsion Technologies for Large Commercial Aircraft," presented at the Electric and Hybrid Aerospace Technology Symposium, Cologne, Germany, 2016.

[13] P. Czyz, T. Guillod, F. Krismer *et al.*, "Exploration of the Design and Performance Space of a High Frequency 166 kW/10 kV SiC Solid-State Air-Core Transformer," in *Proc. of the IEEE Int. Power Electron. Conf. (ECCE Asia)*, 2018.

[14] M. Armstrong, "Superconducting Turboelectric Distributed Aircraft Propulsion," presented at the Cryogenic Engineering Conf. / Int. Cryogenic Materials Conf., 2015.

[15] M. H. Kheraluwala, D. W. Novotny, and D. M. Divan, "Coaxially Wound Transformers for High-Power High-Frequency Applications," *IEEE Trans. Power Electron.*, vol. 7, no. 1, pp. 54–62, 1992.

[16] K. Klontz, D. Divan, and D. Novotny, "An Actively Cooled 120 kW Coaxial Winding Transformer for Fast Charging Electric Vehicles," *IEEE Trans. Ind. Appl.*, vol. 31, no. 6, pp. 1257–1263, 1995.

[17] L. Heinemann, "An Actively Cooled High Power, High Frequency Transformer with High Insulation Capability," in *Proc. of the IEEE Appl. Power Electron. Conf. and Expo. (APEC)*, 2002.

[18] B. Engel, G. Bachmann, A. Falk *et al.*, "15 kV/16.7 Hz Energy Supply System with Medium Frequency - Transformer and 6.5 kV IGBTs in Resonant Operation," in *Proc. of the IEEE European Conf. on Power Electron. and Appl. (EPE)*, 2003.

[19] M. Steiner and H. Reinold, "Medium Frequency Topology in Railway Applications," in *Proc. of the IEEE European Conf. on Power Electron. and Appl. (EPE)*, 2007.

[20] D. Aggeler, J. Biela, and J. W. Kolar, "A Compact, High Voltage 25 kW, 50 kHz DC-DC Converter Based on SiC JFETs," in *Proc. of the IEEE Appl. Power Electron. Conf. and Expo. (APEC)*, 2008.

[21] "UNIFLEX-PM (Advanced Power Converters for Universal and Flexible Power Management in Future Electricity Networks)," https://cordis.europa.eu/project/id/19794/reporting.

[22] T. Kjellqvist, S. Ostlund, S. Norrga *et al.*, "Thermal Evaluation of a Medium Frequency Transformer in a Line Side Conversion System," in *Proc. of the IEEE European Conf. on Power Electron. and Appl. (EPE)*, 2009.

[23] M. Pavlovsky, S. W. H. de Haan, and J. A. Ferreira, "Reaching High Power Density in Multikilowatt DC–DC Converters with Galvanic Isolation," *IEEE Trans. Power Electron.*, vol. 24, no. 3, pp. 603–612, 2009.

[24] Y. Du, S. Baek, S. Bhattacharya *et al.*, "High-Voltage High-Frequency Transformer Design for a 7.2kV to 120V/240V 20kVA Solid State Transformer," in *Proc. of the IEEE Annual Conf. of the Industrial Electron. Society (IECON)*, 2010.

[25] H. Hoffmann and B. Piepenbreier, "Medium Frequency Transformer for Rail Application Using New Materials," in *Proc. of the IEEE Int. Electric Drives Production Conf. (EDPC)*, 2011.

[26] I. Villar, A. Garcia-Bediaga, U. Viscarret *et al.*, "Proposal and Validation of Medium-Frequency Power Transformer Design Methodology," in *Proc. of the IEEE Energy Conv. Congress and Expo. (ECCE USA)*, 2011.

[27] I. Villar, L. Mir, I. Etxeberria-Otadui *et al.*, "Optimal Design and Experimental Validation of a Medium-Frequency 400kVA Power Transformer for Railway Traction Applications," in *Proc. of the IEEE Energy Conv. Congress and Expo. (ECCE USA)*, 2012.

[28] C. Zhao, D. Dujic, A. Mester *et al.*, "Power Electronic Traction Transformer—Medium Voltage Prototype," *IEEE Trans. Ind. Electron.*, vol. 61, no. 7, pp. 3257–3268, 2014.

[29] S. S. Baek, S. Bhattacharya, B. Cougo *et al.*, "Accurate Equivalent Circuit Modeling of a Medium-Voltage and High-Frequency Coaxial Winding DC-link Transformer for Solid State Transformer Applications," in *Proc. of the IEEE Energy Conv. Congress and Expo. (ECCE USA)*, 2012.

[30] G. Ortiz, M. Leibl, J. W. Kolar *et al.*, "Medium Frequency Transformers for Solid-State-Transformer Applications — Design and Experimental Verification," in *Proc. of the IEEE Int. Conf. on Power Electron. and Drive Systems (PEDS)*, 2013.

[31] *STS*, "MF-Transformator für Traktion," www.sts-trafo.de.

[32] D. Rothmund, G. Ortiz, T. Guillod *et al.*, "10kV SiC-Based Isolated DC-DC Converter for Medium Voltage-Connected Solid-State Transformers," in *Proc. of the IEEE Appl. Power Electron. Conf. and Expo. (APEC)*, 2015.

[33] M. A. Bahmani, "Design and Optimization Considerations of Medium-Frequency Power Transformers in High-Power DC-DC Applications," Ph.D. dissertation, Chalmers University of Technology, Gothenburg, Sweden, 2016.

[34] C. Gammeter, F. Krismer, and J. W. Kolar, "Comprehensive Conceptualization, Design, and Experimental Verification of a Weight-Optimized All-SiC 2 kV/700 V DAB for an Airborne Wind Turbine," *IEEE Trans. Emerg. Sel. Topics Power Electron.*, vol. 4, no. 2, pp. 638–656, 2016.

[35] F. Kieferndorf, U. Drofenik, F. Agostini *et al.*, "Modular PET, Two-Phase Air-Cooled Converter Cell Design and Performance Evaluation with 1.7kV IGBTs for MV Applications," in *Proc. of the IEEE Appl. Power Electron. Conf. and Expo. (APEC)*, 2016.

[36] A. Pereira, F. Sixdenier, M. A. Raulet *et al.*, "Comparison between Numerical and Analytical Methods of AC Resistance Evaluation for Medium-Frequency Transformers: Validation on a Prototype and Thermal Impact Analysis," *Canadian J. Elect. Comput. Eng.*, vol. 40, no. 2, pp. 101–109, 2017.

[37] S. Isler, T. Chaudhuri, D. Aguglia *et al.*, "Development of a 100 kW, 12.5 kV, 22 kHz and 30 kV Insulated Medium Frequency Transformer for Compact and Reliable Medium Voltage Power Conversion," in *Proc. of the IEEE European Conf. on Power Electron. and Appl. (EPE)*, 2017.

[38] A. K. Das, Z. Wei, B. G. Fernandes *et al.*, "Multi-Variable Optimization Methodology for Medium-Frequency High-Power Transformer Design Employing Steepest Descent Method," in *Proc. of the IEEE Appl. Power Electron. Conf. and Expo. (APEC)*, 2018.

[39] Q. Chen, R. Raju, D. Dong *et al.*, "High Frequency Transformer Insulation in Medium Voltage SiC enabled Air-Cooled Solid-State Transformers," in *Proc. of the IEEE Energy Conv. Congress and Expo. (ECCE USA)*, 2018.

[40] M. Mogorovic and D. Dujic, "100kW, 10kHz Medium Frequency Transformer Design Optimization and Experimental Verification," *IEEE Trans. Power Electron.*, vol. 34, no. 2, pp. 1696–1708, 2019.

[41] S. Zhao, Q. Li, F. C. Lee *et al.*, "High-Frequency Transformer Design for Modular Power Conversion From Medium-Voltage AC to 400 VDC," *IEEE Trans. Power Electron.*, vol. 33, no. 9, pp. 7545–7557, 2018.

[42] *Delta Electronics*, "High-Efficiency, Medium-Voltage-Input, Solid-State-Transformer-Based 400-kW/1000-V/400-A Extreme Fast Charger for Electric Vehicles," https://www.energy.gov/.

[43] R. L. Da Silva, V. L. F. Borges, C. E. Possamai *et al.*, "Solid-State Transformer for Power Distribution Grid Based on a Hybrid Switched-Capacitor LLC-SRC Converter: Analysis, Design, and Experimentation," *IEEE Access*, vol. 8, pp. 141 182–141 207, 2020.

[44] Z. Li, Y.-H. Hsieh, Q. Li *et al.*, "High-Frequency Transformer Design with High-Voltage Insulation for Modular Power Conversion from Medium-Voltage AC to 400-V DC," in *Proc. of the IEEE Energy Conv. Congress and Expo. (ECCE USA)*, 2020.

[45] M. Kharezy, "A Novel Oil-immersed Medium Frequency Transformer for Offshore HVDC Wind Farms," Ph.D. dissertation, Chalmers University of Technology, Gothenburg, Sweden, 2020.

[46] R. Haneda and H. Akagi, "Design and Performance of the 850-V 100-kW 16-kHz Bidirectional Isolated DC–DC Converter using SiC-MOSFET/SBD H-Bridge Modules," *IEEE Trans. Power Electron.*, vol. 35, no. 10, pp. 10 013–10 025, 2020.

[47] Z. Guo, R. Yu, W. Xu *et al.*, "Design and Optimization of a 200-kW Medium-Frequency Transformer for Medium-Voltage SiC PV Inverters," *IEEE Trans. Power Electron.*, vol. 36, no. 9, pp. 10 548–10 560, 2021.

[48] P. Czyz, T. Guillod, F. Krismer *et al.*, "Design and Experimental Analysis of 166 kW Medium-Voltage Medium-Frequency Air-Core Transformer for 1:1-DCX Applications," *IEEE Trans. Emerg. Sel. Topics Power Electron.*, early access, 2021.

[49] J. Fabre, P. Ladoux, H. Caron *et al.*, "Characterization and Implementation of Resonant Isolated DC/DC Converters for Future MVDC Railway Electrification Systems," *IEEE Trans. Transport. Electrific.*, vol. 7, no. 2, pp. 854–869, 2021.

[50] C. Zhao, Y.-H. Hsieh, F. C. Lee *et al.*, "Design and Analysis of a High-Frequency CLLC Resonant Converter with Medium Voltage insulation for Solid-State-Transformer," in *Proc. of the IEEE Appl. Power Electron. Conf. and Expo. (APEC)*, 2021.

[51] T. Guillod, P. Czyz, and J. W. Kolar, "Geometrical Optimization of Medium-Frequency Air-Core Transformers for DCX Applications," *IEEE Trans. Emerg. Sel. Topics Power Electron.*, under review, 2021.

[52] J. W. Kolar, U. Drofenik, J. Biela *et al.*, "PWM Converter Power Density Barriers," in *Proc. of the IEEE Power Conv. Conf. (PCC)*, 2007.

[53] U. Drofenik, "A 150kW Medium Frequency Transformer Optimized for Maximum Power Density," in *Proc. of the IEEE Int. Conf. on Integrated Power Electron. Systems (CIPS)*, 2012.

[54] T. Guillod and J. W. Kolar, "Medium-Frequency Transformer Scaling Laws: Derivation, Verification, and Critical Analysis," *CPSS Trans. on Power Electron. and Appl.*, vol. 5, no. 1, pp. 18–33, 2020.

[55] L. Wang, Q. Zhu, W. Yu *et al.*, "A Medium-Voltage Medium-Frequency Isolated DC–DC Converter Based on 15-kV SiC MOSFETs," *IEEE Trans. Emerg. Sel. Topics Power Electron.*, vol. 5, no. 1, pp. 2168–6785, 2017.

[56] Q. Zhu, L. Wang, L. Zhang *et al.*, "A 10 kV DC Transformer (DCX) Based on Current Fed SRC and 15 kV SiC MOSFETs," in *Proc. of the IEEE Appl. Power Electron. Conf. and Expo. (APEC)*, 2018.

[57] T. Guillod, D. Rothmund, and J. W. Kolar, "Active Magnetizing Current Splitting ZVS Modulation of a 7kV/400V DC Transformer," *IEEE Trans. Power Electron.*, vol. 35, no. 2, pp. 1293–1305, 2019.

[58] S. Inoue and H. Akagi, "A Bidirectional Isolated DC–DC Converter as a Core Circuit of the Next-Generation Medium-Voltage Power Conversion System," *IEEE Trans. Power Electron.*, vol. 22, no. 2, pp. 535–542, 2007.

[59] *Cree/Wolfspeed*, "QPM3-10000-0300, Z-FET Silicon Carbide MOSFET," Oct. 2017.

[60] J. B. Casady, V. Pala, D. J. Lichtenwalner *et al.*, "New Generation 10kV SiC Power MOSFET and Diodes for Industrial Applications," in *Proc. of the Int. Exhib. and Conf. for Power Electron., Intelligent Motion, Renewable Energy and Energy Manag. (PCIM Europe)*, 2015.

[61] D. Rothmund, D. Bortis, J. Huber *et al.*, "10kV SiC-based Bidirectional Soft-Switching Single-Phase AC/DC Converter Concept for Medium-Voltage Solid-State Transformers," in *Proc. of the IEEE Int. Symposium on Power Electron. for Distrib. Generation Syst. (PEDG)*, 2017.

[62] D. Rothmund, D. Bortis, and J. W. Kolar, "Accurate Transient Calorimetric Measurement of Soft-Switching Losses of 10-kV SiC MOSFETs and Diodes," *IEEE Trans. Power Electron.*, vol. 33, no. 6, pp. 5240–5250, 2018.

[63] *Celem*, "CSP 120/200 Conduction-Cooled Capacitor," Nov. 2019.

[64] *FTCAP GmbH*, "Film Capacitors," https://www.ftcap.de/en/downloads/.

[65] R. Bosshard, J. W. Kolar, J. Muehlethaler *et al.*, "Modeling and η-γ-Pareto Optimization of Inductive Power Transfer Coils for Electric Vehicles," *IEEE Trans. Emerg. Sel. Topics Power Electron.*, vol. 3, no. 1, pp. 50–64, 2015.

[66] T. Guillod, F. Krismer, and J. W. Kolar, "Magnetic Equivalent Circuit of MF Transformers: Modeling and Parameter Uncertainties," *Electr Eng*, vol. 100, pp. 2261–2275, 2018.

[67] C. Sullivan, "Optimal Choice for Number of Strands in a Litz-Wire Transformer Winding," *IEEE Trans. Power Electron.*, vol. 14, no. 2, pp. 283–291, 1999.

[68] M. Leibl, G. Ortiz, and J. W. Kolar, "Design and Experimental Analysis of a Medium-Frequency Transformer for Solid-State Transformer Applications," *IEEE Trans. Emerg. Sel. Topics Power Electron.*, vol. 5, no. 1, pp. 110–123, 2017.

[69] T. Guillod, J. Huber, F. Krismer *et al.*, "Litz Wire Losses: Effects of Twisting Imperfections," in *Proc. of the IEEE Workshop on Control and Modeling for Power Electron. (COMPEL)*, 2017.

[70] T. B. Gradinger and U. Drofenik, "Managing High Currents in Litz-Wire-Based Medium-Frequency Transformers," in *Proc. of the IEEE European Conf. on Power Electron. and Appl. (EPE)*, 2018.

[71] *Dow Corning*, "TC4605 HLV, Thermally Conductive Encapsulant," 2015.

[72] M. Leibl, "Three-Phase Rectifier and High-Voltage Generator for X-Ray Systems," Ph.D. dissertation, ETH Zurich, Zurich, Switzerland, 2017.

[73] T. Guillod, "Modeling and Design of Medium-Frequency Transformers for Future Medium-Voltage Power Electronics Interfaces," Ph.D. dissertation, ETH Zurich, Zurich, Switzerland, 2018.

[74] J. Muehlethaler, "Modeling and Multi-Objective Optimization of Inductive Power Components," Ph.D. dissertation, ETH Zurich, Zurich, Switzerland, 2012.

[75] J. Muehlethaler, J. W. Kolar, and A. Ecklebe, "A Novel Approach for 3D Air Gap Reluctance Calculations," in *Proc. of the IEEE Int. Power Electron. Conf. (ECCE Asia)*, 2011.

[76] K. Venkatachalam, C. Sullivan, T. Abdallah *et al.*, "Accurate Prediction of Ferrite Core Loss with Nonsinusoidal Waveforms using only Steinmetz Parameters," in *Proc. of the IEEE Workshop on Comp. in Power Electron.*, 2002.

[77] R. M. Burkart, "Advanced Modeling and Multi-Objective Optimization of Power Electronic Converter Systems," Ph.D. dissertation, ETH Zurich, Zurich, Switzerland, 2016.

[78] T. Guillod, R. Faerber, D. Rothmund *et al.*, "Dielectric Losses in Dry-Type Insulation of Medium-Voltage Power Electronic Converters," *IEEE Trans. Emerg. Sel. Topics Power Electron.*, vol. 8, no. 3, pp. 2716–2732, 2020.

[79] M. Mogorovic and D. Dujic, "Thermal Modeling and Experimental Verification of an Air Cooled Medium Frequency Transformer," in *Proc. of the IEEE European Conf. on Power Electron. and Appl. (EPE)*, 2017.

[80] B. Carsten, "Increasing Transformer Power Density through Thermal Management," presented at the ECPE Workshop on Design of Magnetic Components, Munich, Germany, 2012.

[81] G. Ortiz, "High-Power DC-DC Converter Technologies for Smart Grid and Traction Applications," Ph.D. dissertation, ETH Zurich, Zurich, Switzerland, 2014.

[82] B. Cougo, A. Tuysüz, J. Muehlethaler *et al.*, "Increase of Tape Wound Core Losses Due to Interlamination Short Circuits and Orthogonal Flux Components," in *Proc. of the IEEE Annual Conf. of the Industrial Electron. Society (IECON)*, 2011.

[83] J. Szynowski, R. Kolano, A. Kolano-Burian *et al.*, "Reduction of Power Losses in the Tape-Wound FeNiCuNbSiB Nanocrystalline Cores Using Interlaminar Insulation," *IEEE Trans. Magn.*, vol. 50, no. 4, pp. 1–4, 2014.

[84] *Safety Requirements for Power Electronic Converter Systems and Equipment. Part 1: General*, IEC Std. 62 477-1, 2012.

[85] *Safety Requirements for Power Electronic Converter Systems and Equipment - Part 2: Power Electronic Converters from 1 000 V AC or 1 500 V DC up to 36 kV AC or 54 kV DC*, IEC Std. 62 477-2, 2018.

[86] *Guidelines for Limiting Exposure to Time-Varying Electric and Magnetic Fields (1 Hz to 100 kHz)*, International Commission on Non-Ionizing Radiation Protection Std. ICNIRP, 2010.

[87] T. Guillod, F. Krismer, and J. W. Kolar, "Electrical Shielding of MV/MF Transformers Subjected to High dv/dt PWM Voltages," in *Proc. of the IEEE Appl. Power Electron. Conf. and Expo. (APEC)*, 2017.

[88] P. Wallmeier and H. Grotstollen, "Magnetic Shielding Applied to High-Frequency Inductors," in *Proc. of the IEEE Industry Appl. Society Annual Meeting*, 1997.

[89] R. P. Clayton, *Introduction to Electromagnetic Compatibility*. John Wiley & Sons, 2006.

[90] C. Gammeter, F. Krismer, and J. W. Kolar, "Weight Optimization of a Cooling System Composed of Fan and Extruded-Fin Heat Sink," *IEEE Trans. Ind. Appl.*, vol. 51, no. 1, pp. 509–520, 2015.

[91] R. Bosshard, "Multi-Objective Optimization of Inductive Power Transfer Systems for EV Charging," Ph.D. dissertation, ETH Zurich, Zurich, Switzerland, 2016.

[92] A. Cremasco, D. Rothmund, M. Curti *et al.*, "Voltage Distribution in the Windings of Medium-Frequency Transformers Operated with Wide Bandgap Devices," *IEEE Trans. Emerg. Sel. Topics Power Electron.*, early access, 2021.

[93] *Ferroxcube*, "3C94 Material Specification," Sep. 2008.

[94] D. Neumayr, D. Bortis, J. W. Kolar *et al.*, "Origin and Quantification of Increased Core Loss in MnZn Ferrite Plates of a Multi-Gap Inductor," *CPSS Trans. on Power Electron. and Appl.*, vol. 4, no. 1, pp. 72–93, 2019.

[95] P. Papamanolis, T. Guillod, F. Krismer *et al.*, "Transient Calorimetric Measurement of Ferrite Core Losses up to 50 MHz," *IEEE Trans. Power Electron.*, vol. 36, no. 3, pp. 2548–2563, 2020.

[96] *Recommended Practice for Testing Insulation Resistance of Electric Machinery*, IEEE Std. 43-2013, 2014.

[97] *Megger*, "Guide To Diagnostic Insulation Testing Above 1 kV," https://megger.com/support/technical-library/.

[98] *Novocontrol*, "Alpha-A High Performance Modular Measurement System," https://www.novocontrol.de/php/ana_alpha.

[99] R. Faerber, "Endurance of Polymeric Insulation under Mixed-Frequency Medium-Voltage Stress," Ph.D. dissertation, ETH Zurich, Zurich, Switzerland, 2019.

Piotr Czyz (S'14) received his B.Sc. and M.Sc. (summa cum laude) degrees in Electrical Engineering from the Gdansk University of Technology, in 2014 and 2015, respectively. In 2016 he was with C&T Elmech, Poland, working on the development of uninterruptible power supplies. In 2017 he began his Ph.D. at the Power Electronic Systems Laboratory (PES) at ETH Zurich and passed the doctoral examination in 2021. His research interests lie in the field of medium-voltage solid-state transformers technologies with the focus on medium-frequency transformers and power semiconductor stages.

This article has been accepted for publication in IEEE Journal of Emerging and Selected Topics in Power Electronics. This is the author's version which has not been fully edited and content may change prior to final publication. Citation information: DOI 10.1109/JESTPE.2021.3123793

Thomas Guillod (M'18) received the M.Sc. and Ph.D. degree in electrical engineering from the Swiss Federal Institute of Technology (ETH) Zurich, Switzerland with a focus on power electronics, numerical analysis, and field theory, in 2013 and 2018, respectively. After a postdoc at the Power Electronic Systems Laboratory (ETH Zurich, Switzerland), he was working as an independent engineering consultant for both industrial and academic projects. In 2021, he joined that the Thayer School of Engineering at Dartmouth College, NH, USA as a research associate. His current research interests include high-frequency magnetic components, high-frequency power magnetic materials, and advanced numerical modeling techniques.

Daifei Zhang received the B.Sc. degree in Electrical Engineering and Automation from Huazhong University of Science and Technology (HUST) in 2017, and the M.Sc. degree in Electrical Engineering and Information Technology from ETH Zurich in 2019. In 2017, he was with the Institute for Power Generation and Storage Systems in RWTH Aachen, Germany as an exchange student. In July 2019, he joined the Power Electronic Systems Laboratory (PES), ETH Zurich as a Ph.D. student, focusing on advanced three-phase power electronics inverters and rectifiers.

Florian Krismer (M'12) received the Dipl.-Ing. (M.Sc.) degree in electrical engineering with specialization in automation and control technology from the Vienna University of Technology, Vienna, Austria, in 2004, and the Ph.D. degree in electrical engineering from the Department of Information Technology and Electrical Engineering of ETH Zurich, Zurich, Switzerland, in 2010. He is currently a Research Associate at PES, where he has cosupervised Ph.D. students and has continued with his research in the field of power electronics. He is the author or coauthor of numerous conference and peer-review publications and has received two awards for his publications. His research interests include the analysis, design, and general optimization of power converter systems, e.g., the weight optimization of a bi-directional dc–dc converter for an airborne wind turbine. Furthermore, he conducts research related to the filtering of conducted electromagnetic emissions and collaborated in the littlebox-challenge with respect to the hardware realization.

Jonas Huber (S'11–M'16) is a senior researcher at the Power Electronic Systems Laboratory of the Federal Institute of Technology (ETH) Zurich, Switzerland. He received the MSc (with distinction) degree and the PhD degree from ETH Zurich, Switzerland, in 2012 and 2016, respectively. Since 2012, he has been with the Power Electronic Systems Laboratory, ETH Zurich and became a Postdoctoral Researcher, focusing his research interests on the field of solid-state transformers, specifically on the analysis, optimization, and design of high-power multi-cell converter systems, reliability considerations, control strategies, and applicability aspects. In 2017, he joined ABB Switzerland Ltd. as an R&D Engineer designing high-power DC-DC converter systems for traction applications. He then returned to the Power Electronic Systems Laboratory as a Senior Researcher in 2020, extending his research scope to all types of WBG-semiconductor-based ultra-compact, ultra-efficient or highly dynamic converter systems. He is a member of the IEEE Power Electronics Society.

Raphael Färber (S'16) received a M.Sc. degree in physics from the Ecole Polytechnique Fédérale de Lausanne (EPFL), Switzerland. He holds a Ph.D. degree from ETH Zurich, Switzerland, where he is currently a postdoctoral researcher at the High Voltage Laboratory. His research interests include the characterization and understanding of charge transport in solid and gaseous dielectrics, with a current focus on partial discharge phenomena under transient voltages.

Christian M. Franck (SM´11) received the Diploma degree in physics from the University of Kiel, Germany, in 1999, and the Ph.D. degree in physics from the University of Greifswald, Germany, in 2003. From 2003 to 2009, he was with the ABB Swiss Corporate Research Center, Baden Dättwil, Switzerland, as a Scientist and a Group Leader for gas circuit breakers and high-voltage systems. He is currently a Full Professor of high-voltage engineering with ETH Zürich, Switzerland. His current main research interests include gaseous and solid insulation systems and switching arcs.

Johann W. Kolar (M´89–F´10) received his M.Sc. and Ph.D. degree (summa cum laude) from the University of Technology Vienna, Austria, in 1997 and 1999, respectively. Since 1984, he has been working as independent researcher and international consultant in close collaboration with the Vienna University of Technology, in the fields of power electronics, industrial electronics and high performance drive systems. He was appointed Assoc. Professor and Head of the Power Electronic Systems Laboratory at the Swiss Federal Institute of Technology (ETH) Zurich on Feb. 1, 2001, and was promoted to the rank of Full Prof. in 2004. Dr. Kolar has proposed numerous novel converter concepts incl. the Vienna Rectifier, the Sparse Matrix Converter and the Swiss Rectifier, has spearheaded the development of x-million rpm electric motors, and has pioneered fully automated multi-objective power electronics design procedures. He has graduated 80 Ph.D. students, has published 900+ journal and conference papers and 4 book chapters, and has filed 200+ patents. He has presented 35+ educational seminars at leading international conferences and has served as IEEE PELS Distinguished Lecturer from 2012 – 2016. He has received 35+ IEEE Transactions and Conference Prize Paper Awards, the 2014 IEEE Power Electronics Society R. David Middlebrook Achievement Award, the 2016 IEEE PEMC Council Award, the 2016 IEEE William E. Newell Power Electronics Award, the 2020 EPE Outstanding Achievement Award and 2 ETH Zurich Golden Owl Awards for excellence in teaching. He was elected to the U.S. National Academy of Engineering as an international member in 2021. The focus of his current research is on ultra-compact/efficient WBG PFC rectifier and inverter systems, ultra-high BW switch-mode power amplifiers, multi-port converters, Solid-State Transformers, multi-functional actuators, ultra-high speed / motor-integrated drives, bearingless motors, ANN-based multi-objective design optimization and sustainable systems.